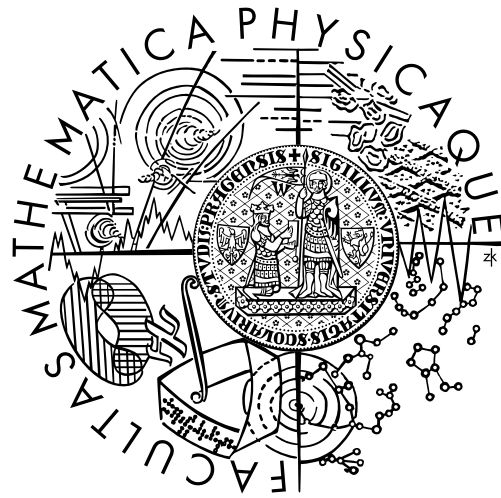Charles University in Prague

Faculty of Mathematics and Physics

DIPLOMA THESIS

Michal Grochol

Luminescence spectroscopy of semiconductor quantum structures

Institute of Physics of Charles University

Supervisor:

Assoc. Prof. Roman Grill PhD.

Study program:

Physics, Optics and optoelectronics, Optoelectronics and photonics

Acknowledgement

I would like to thank all the people who helped me with this work. The most I would like to thank to my supervisor Assoc. Prof. Roman Grill PhD. for the valuable advices and consultations. I would also like to thank to Assoc. Prof. Jiří Bok PhD. for numerical advices and Prof. Ivan Barvík PhD. for theoretical consultations.

I confess that I have written my diploma thesis on my own and using only the quoted sources. I agree with lending the diploma thesis.

Prague, April 17, 2003

Michal Grochol

Název práce: Lumiscenční spektroskopie polovodičových kvantových struktur

Autor: Michal Grochol

Katedra (ústav): Fyzikální ústav Univerzity Karlovy

Vedoucí diplomové práce: Doc. RNDr. Roman Grill, CSc.

e-mail vedoucího: grill@karlov.mff.cuni.cz

Abstrakt:

Cílem této práce bylo spočítat disperzní relaci excitonu v dvojité kvantové jámě v obecném magnetickém a elektrickém poli metodou těsné vazby a rozvojem vlnové funkce do vlastních funkcí momentu hybnosti. Ze získaných disperzních relací a vlnových funkcí byly spočítány pravděpodobnosti přechodů, hustota stavů a teoretická luminiscenční spektra. Zjistili jsme, jak se projevuje singularita v excitoné hustotě stavů v luminiscenčních spektrech. Také jsme se zabývali možností vzniku excitonové kapaliny.

Klíčová slova: Dvojitá kvantová jáma v magnetickém poli, GaAs/GaAlAs, Luminiscence, Exciton

Title: Luminescence spectroscopy of semiconductor quantum structures

Author: Michal Grochol

Department: Institute of Physics of Charles University

Supervisor: Assoc. Prof. Roman Grill, PhD.

Supervisor's e-mail address: grill@karlov.mff.cuni.cz

Abstract:

The aim of this work was to compute the dispersion relation of the exciton in the double quantum well in the magnetic and electric field by the tight-binding method and by the expansion of the wave function into eigenfunctions of the angular momentum. Using calculated dispersion relations and wave functions we calculated the probabilities of transition, density of states and luminescence spectra. We have found out how the singularity in the exciton density of states manifests in the luminescence spectra. The possibility of the formation of excitonic liquid is also mentioned.

Keywords: Double quantum well in magnetic field, GaAs/GaAlAs, Luminescence, Exciton

Contents

Chapter 1

Introduction

1.1 Overview

The two-dimensional semiconductor heterostructures like modulation doped heterostructures, quantum wells and superlattices have attracted the attention for a long time and have found many application e.g. in the semiconductor lasers, HEMTs, LEDs etc. The development of the growth technologies for theses structures like molecular beam epitaxy (MBE) and metal oxide chemical vapour deposition (MOCVD) enabled a significant improvement of the sample quality and thus stimulated further experimental and theoretical research.

Quantum wells have attracted attention since their first fabrication in 1973. Due to their unique properties, especially strong dependence of transport and optical properties on the applied magnetic and electric field, double quantum wells (DQW) are investigated in an intensive way nowadays. The mostly used material for fabricating these structures is GaAs/GaAlAs thanks to its properties, e.g. practically the same lattice constant of GaAs and AlAs. Typical parameters of AlGaAs based semiconductors are listed in Table 2.1.

Perpendicular magnetic field is studied the most, since Landau levels appear (if we neglect electron-hole interaction). Landau levels are on the origin of Quantum Hall effect, which was discovered in low dimensional quantum structures and has already found many applications, in the first place in metrology as a resistance standard. Parallel magnetic field is also of interest since a singularity in the electron density of states in this field was discovered [1] and then experimentally measured [2], [3].

Excitons play a significant role in DQW and they have been treated so far predominantly by variational approach [4], [2] in the electric field. Recently described theoretical treatment of the magnetoexcitons [5] is the basis of our approach. The influence of parallel and perpendicular magnetic field on the exciton dispersion relation is significant and various interesting effects can be observed as a shift of the minimum of the dispersion relation away off the origin, or the appearance of a new kind of van Hove logarithmic singularity in the exciton density of states or the increase of the effective

mass of the exciton [6]. The possible applications of the exciton dispersion relation like the saser development [7] or the conditions for Bose condensation of the excitons, which has already been measured [8], are mentioned. All these new effects together with our results are in detail discussed in chapter 7.

1.2   Objectives

The aim of this work is to develop an efficient way for solving a Schrödinger equation of the exciton in DQW and thus calculate the density of states and mainly the theoretical luminescence spectra which could be then compared to experimental results. Since Institute of Physics of Charles University has samples grown by MBE from the Academy of Sciences of the Czech Republic and from the University of Erlangen the developed method should be used for efficient designing of new samples with optimized parameters to make the best of the capacity of the optical laboratory of Institute of Physics to measure and verify as much predictions as possible.

Chapter 2

Band structure of bulk III-V compounds

The theory of next three chapters is taken mainly from [9].

2.1 Crystalline and electronic properties

The III-V compounds crystallize in the sphalerite structure. The first Brillouin zone of the reciprocal lattice is a truncated octahedron (see Fig. 2.1). Several high symmetry points or lines of the first Brillouin zone have received specific notations, e.g. X, L and Γ points. In a III-V binary material like GaAs, there are 8 electrons per unit cell (3 from Ga and 5 from As) which contribute to the chemical bounds. We can say that the orbital of every atom hybridize (due to interaction with his neighbours) to form bonding and antibonding state which broaden into bands because of a great number of unit cells interacting. Two electrons fill the s band and remaining six electrons occupy the p bands. Antibonding bands are empty and the lowest lying one forms the conduction band. All III-V compounds have the top of the valence band in the center of Brillouin zone (in point Γ). The spin-orbit coupling lowers the sixfold degeneracy in the point Γ, and gives rise to a quadruplet with $J = 3/2$ (symmetry Γ_8) and a doublet $J = 1/2$ (symmetry Γ_7). The conduction band edge of the III-V materials is situated near one of the points Γ, L or X. The heavier the cation the more likely it is to find band edge at the point Γ.

2.2 $\vec{k}.\vec{p}$ analysis

In a bulk crystal the one-electron Schrödinger equation takes form of:

$$\left[\frac{p^2}{2m_0} + V(\mathbf{r}) + \frac{\hbar^2}{4m_0^2 c^2} \left(\sigma \times \nabla V \right) . \mathbf{p} + H_r \right] \Psi(\mathbf{r}) = E\Psi(\mathbf{r}). \tag{2.1}$$
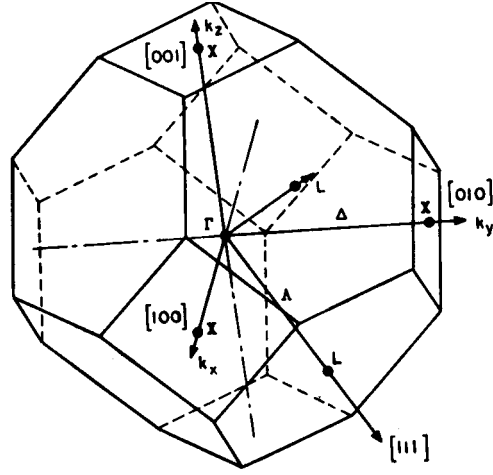
Figure 2.1: First Brillouin zone of face-centred cubic lattice, taken from [9].

$V(\mathbf{r})$ is the crystalline potential which includes an average of the electron-electron interaction and is periodic with the period of the Bravais lattice. The third term is the spin-orbit coupling and the fourth term is the relativistic correction (mass-velocity and Darwin term). The solution of eq. (2.1) can be written in the Bloch form:

$$\Psi_{n\mathbf{k}}(\mathbf{r}) = N u_{n\mathbf{k}}(\mathbf{r}) \exp(i\mathbf{k}.\mathbf{r}), \tag{2.2}$$

where N is a normalization coefficient and $u_{n\mathbf{k}}(\mathbf{r})$ is a periodic function of $\mathbf{r}$ with the period of the lattice. The periodic parts of the Bloch functions $u_{n\mathbf{k}}(\mathbf{r})$ are the solutions of (dropping the relativistic corrections)

$$\left[\frac{p^2}{2m_0} + V(\mathbf{r}) + \frac{\hbar^2}{4m_0^2c^2}(\sigma \times \nabla V).\mathbf{p}+ \right.$$
$$\left. +\frac{\hbar^2 k^2}{2m_0} + \frac{\hbar\mathbf{k}}{2m_0}\left(\mathbf{p} + \frac{\hbar^2}{4m_0^2c^2}(\sigma \times \nabla V)\right)\right] u_{n\mathbf{k}}(\mathbf{r}) = \varepsilon_{n\mathbf{k}}u_{n\mathbf{k}}(\mathbf{r}). \tag{2.3}$$

The $\mathbf{k}$-dependent terms in (2.3) vanish at $\mathbf{k}=0$ and commute with the translation operator. It means that we can write

$$u_{n\mathbf{k}}(\mathbf{r}) = \sum_m c_m(\mathbf{k})u_{m\mathbf{0}}(\mathbf{r}). \tag{2.4}$$

By inserting (2.4) into (2.3), multiplying by $u_{n\mathbf{0}}^*(\mathbf{r})$ and integrating over a unit cell we obtain:

$$\sum_m \left\{\left(\varepsilon_{n\mathbf{0}} - \varepsilon_{n\mathbf{k}} + \frac{\hbar^2 k^2}{2m_0}\right)\delta_{nm} + \frac{\hbar\mathbf{k}}{m_0}.\langle n\mathbf{0}|\mathbf{p} + \frac{\hbar^2}{4m_0^2c^2}(\sigma \times \nabla V)|m\mathbf{0}\rangle\right\} c_m(\mathbf{k}) = 0,$$
$$\tag{2.5}$$

Table 2.1: Parameters of AlGaAs based semiconductors according to [10], [9], [11].

	GaAs	**Al$_x$Ga$_{1-x}$As**	**AlAs**
ε_0 [eV]	1.5192	$1.5192 + 1.247x$ ($x < 0.45$)	3.13
a [nm]	5.6533	$5.6533 + 0.0078x$	5.6611
$\frac{m_{\Gamma_6}}{m_0}$	0.0665	$0.0665 + 0.0835x$	0.15
$\frac{m_{lh}}{m_0}$	0.094	$0.094 + 0.043x$	0.137
$\frac{m_{hh}}{m_0}$	0.34*	$0.34 + 0.42x$	0.76
$\frac{m_{SO}}{m_0}$	0.15	$0.15 + 0.09x$	0.24
Δ [eV]	0.341		0.275
Bandgap	Direct	Direct pro $x < 0.45$	Indirect

*Mean value - Heavy hole band of GaAs is not rotationally parabolic.

where

$$\langle n\mathbf{0}|A|m\mathbf{0}\rangle = \int_{\text{unit cell}} u_{n\mathbf{0}}^*(\mathbf{r})Au_{m\mathbf{0}}(\mathbf{r})d^3r. \tag{2.6}$$

Eq. (2.5) is well suited for the perturbation approach. Supposing that the nth band edge is non degenerate, we can then assume for small $\mathbf{k}$:

$$c_n(\mathbf{k}) \sim 1; \qquad c_m(\mathbf{k}) = \alpha.\mathbf{k}, \tag{2.7}$$

which inserted in eq. (2.5), results in:

$$c_m(\mathbf{k}) = \frac{\hbar\mathbf{k}}{m_0}.\mathbf{\Pi_{nm}}\frac{1}{\varepsilon_{n\mathbf{0}} - \varepsilon_{m\mathbf{0}}} \tag{2.8}$$

and gives the second order correction to $\varepsilon_{n\mathbf{0}}$:

$$\varepsilon_{n\mathbf{k}} = \varepsilon_{n\mathbf{0}} + \frac{\hbar^2 k^2}{2m_0} + \frac{\hbar^2}{m_0}\sum_{m\neq n}\frac{|\mathbf{\Pi_{nm}}.\mathbf{k}|^2}{\varepsilon_{n\mathbf{0}} - \varepsilon_{m\mathbf{0}}}. \tag{2.9}$$

The vector $\mathbf{\Pi}$ is defined as:

$$\mathbf{\Pi} = \mathbf{p} + \frac{\hbar^2}{4m_0^2c^2}(\sigma \times \nabla V). \tag{2.10}$$

As long as $\mathbf{k}$ is small ($\varepsilon_{n\mathbf{k}}-\varepsilon_{n\mathbf{0}}$ remains much smaller than all band edge gaps $\varepsilon_{n\mathbf{0}}-\varepsilon_{m\mathbf{0}}$) the dispersion relations of the non degenerate bands are parabolic in $\mathbf{k}$ in the vicinity of the Γ point.

$$\varepsilon_{n\mathbf{k}} = \varepsilon_{n\mathbf{0}} + \frac{\hbar^2}{m_0}\sum_{\alpha,\beta}k_\alpha\frac{1}{\mu_n^{\alpha\beta}}k_\beta, \tag{2.11}$$

where

$$\frac{1}{\mu_n^{\alpha\beta}} = \frac{1}{m_0}\delta_{\alpha\beta} + \frac{2}{m_0^2}\sum_{m\neq n}\frac{\Pi_{mn}^\alpha\Pi_{nm}^\beta}{\varepsilon_{n\mathbf{0}} - \varepsilon_{m\mathbf{0}}}, \tag{2.12}$$

$\mu_n^{\alpha\beta}$ is the effective mass tensor which describes the carrier kinematics in the vicinity of the zone centre and for the energy close to the nth band edge. Assuming the validity of eq. (2.12) the overall effects of the band structure are embodied in the use of an effective mass instead of the free electron mass. The notion of the effective mass is at the heart of the semiclassical description of the carrier motion in a semiconductor.

2.3 Electrons and holes

It can be shown that if an external force $\mathbf{F}$ is applied on the carrier, the equation of motion takes form of:

$$\hbar\frac{d\mathbf{k}}{dt} = \mathbf{F} \tag{2.13}$$

and the carrier velocity in the Bloch state is equal to

$$\mathbf{v} = \frac{1}{\hbar}\frac{\partial\varepsilon_n}{\partial\mathbf{k}}. \tag{2.14}$$

Assuming the external force weak enough to preclude any interband transitions and using eq. (2.12) we can write:

$$v_\alpha = \frac{1}{\hbar}\sum_\beta\left(\frac{1}{\mu_n^{\alpha\beta}} + \frac{1}{\mu_n^{\beta\alpha}}\right)k_\beta. \tag{2.15}$$

$\mu_n^{\alpha\beta}$ is the simplest for the antibonding s orbital since it is a positive scalar:

$$\frac{1}{\mu_{\Gamma_6}^{\alpha\beta}} = \frac{1}{m_{\Gamma_6}}\delta_{\alpha\beta}; \qquad \alpha, \beta = x, y, z \tag{2.16}$$

$$\frac{1}{m_{\Gamma_6}} = \frac{1}{m_0} + \frac{2}{m_0^2}\sum_{m\neq\Gamma_6}\frac{|\pi_{\Gamma_6 m}^z|^2}{\varepsilon_{\Gamma_6} - \varepsilon_{m0}}. \tag{2.17}$$

The effective mass of the topmost occupied valence band is negative (due to coupling with higher band edges) and if an electromagnetic force is applied we can analyze the motion as the motion of fictitious particles characterized by a positive effective mass and a positive charge.

Let us calculate the electric current density. If the carrier velocity in the Bloch state is $\mathbf{v}_k$ then

$$\mathbf{J}_k = -\frac{e}{\Omega}\mathbf{v}_k. \tag{2.18}$$

The total current is the sum over all occupied states. Using the distribution function $f_e(\mathbf{k})$ of the electrons (which would be Fermi-Dirac distribution function at thermal equilibrium) we can write for a single populated band:

$$\mathbf{J} = -\frac{e}{\Omega} \sum_{\mathbf{k}} \mathbf{v}_k f_e(\mathbf{k}), \tag{2.19}$$

where Ω is the crystal volume. If the band is partially occupied, we can write:

$$\mathbf{J} = -\frac{e}{\Omega} \sum_{\mathbf{k}} \mathbf{v}_k + \frac{e}{\Omega} \sum_{\mathbf{k}} \mathbf{v}_k (1 - f_e(\mathbf{k})). \tag{2.20}$$

The first term is zero because the band is filled. The second term can be interpreted as the current of fictitious particles called holes with a positive charge and a distribution function $f_h(\mathbf{k}) = 1 - f_e(\mathbf{k})$. We can write the distribution function explicitly in isotropic parabolic bands at thermal equilibrium:

$$f_h(\mathbf{k}) = \frac{1}{1 + \exp[\frac{1}{k_B T}(\frac{\hbar^2 k^2}{2m_\nu} - \xi)]} \qquad \xi = \varepsilon_\nu - \mu. \tag{2.21}$$

The chemical potential of the holes measured from the valence edge is equal to the electron chemical potential measured from the same edge with the opposite sign.

2.4 Kane model

We restrict our effort to diagonalize the terms with $\mathbf{k} \neq 0$ in eq. (2.3). Due to a non zero spin-orbit coupling in III-V compounds we form linear combinations of the 8 band edge Bloch functions such as to diagonalize eq. (2.3) at $\mathbf{k} = 0$. Such a linear combination is the eigenfunction of the total angular momentum $\mathbf{J} = \mathbf{L} + \sigma$ and its projection J_z. For the S edge $J = 1/2$ (Γ_6 symmetry) and for the P edges we have either $J = 3/2$ or $1/2$. The quadruplet $J = 3/2$ is always higher in energy than the doublet $J = 1/2$ in III-V compound. The quadruplet has the Γ_8 symmetry and the doublet the Γ_7 symmetry. Each edge is twice degenerate due to m_J which are eigenvalues of J_z. The energy separation of the edges can be seen in Fig. 2.2. We project the terms with $\mathbf{k} \neq 0$ in eq. (2.3) on our basis and get a matrix 8×8. The equation for eigenvalues $\varepsilon(\mathbf{k})$ of this matrix can be written as:

$$\varepsilon_0 = \varepsilon_{\Gamma_6} - \varepsilon_{\Gamma_8} \qquad ; \qquad \Delta = \varepsilon_{\Gamma_8} - \varepsilon_{\Gamma_7} \tag{2.22}$$

$$P = \frac{-i}{m_0} \langle S | p_x | X \rangle = \frac{-i}{m_0} \langle S | p_y | Y \rangle = \frac{-i}{m_0} \langle S | p_z | Z \rangle \tag{2.23}$$

$$\lambda(\mathbf{k}) = \varepsilon(\mathbf{k}) - \frac{\hbar^2 k^2}{2m_0}. \tag{2.24}$$
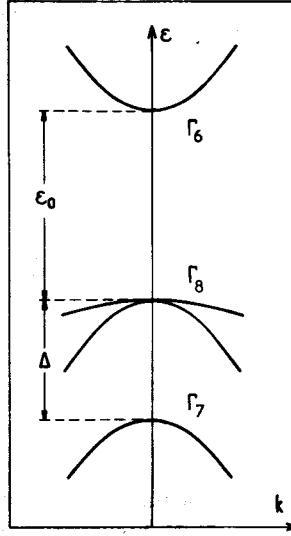
Figure 2.2: Band structure of a direct gap III-V in the vicinity of the zone centre, taken from [9].

S represents s function and X,Y,Z are p functions and finally:

$$\lambda(\mathbf{k}) = -\varepsilon_0 \tag{2.25}$$

or

$$\lambda(\mathbf{k})[\lambda(\mathbf{k}) + \varepsilon_0][\lambda(\mathbf{k}) + \varepsilon_0 + \Delta] = \hbar^2 k^2 P^2 \left[\lambda(\mathbf{k}) + \varepsilon_0 + \frac{2}{3}\Delta \right]. \tag{2.26}$$

We see that $\varepsilon(\mathbf{k})$ depends only on $|\mathbf{k}|$.
If we take $\mathbf{k} \| \mathbf{J} \| \mathbf{z}$, then for $m = \pm\frac{3}{2}$ we obtain a state associated with heavy particles with effective mass equal to the bare electron mass. The $m = \pm\frac{1}{2}$ states are associated with light particles. In the vicinity of the band edges ($\varepsilon = 0$, $\varepsilon = -\varepsilon_0$, $\varepsilon = -\varepsilon_0 - \Delta$) we can expand eq. (2.26) in $\mathbf{k}$ and we find for the effective masses:

$$\frac{1}{m_{\Gamma_6}} = \frac{1}{m_0} + \frac{4P^2}{3\varepsilon_0} + \frac{2P^2}{3(\varepsilon_0 + \Delta)} \tag{2.27}$$

$$\frac{1}{m_{\Gamma_8}^l} = \frac{1}{m_0} - \frac{4P^2}{3\varepsilon_0} \tag{2.28}$$

$$\frac{1}{m_{\Gamma_7}} = \frac{1}{m_0} - \frac{2P^2}{3(\varepsilon_0 + \Delta)}, \tag{2.29}$$

$m_{\Gamma_6} > 0$ and $m_{\Gamma_8}^l, m_{\Gamma_7} < 0$.
Eq. (2.26) is an implicit equation for $\lambda(\mathbf{k})$ versus $\mathbf{k}$ but is explicit for $\mathbf{k}$ versus $\lambda(\mathbf{k})$. We notice that parabolic dispersion law is valid only for small $\mathbf{k}$, when increasing $\mathbf{k}$

Table 2.2: Values of $E_p = 2m_0 P^2$ in eV in some III-V materials, taken from [9].

material	E_p
InP	17.00
InAs	21.11
InSb	22.49
GaAs	22.71
GaSb	22.88

the conduction band effective mass increases. This is called the band non-parabolicity. The fact that the heavy particle states are dispersionless is one of the main drawbacks of restricting of the **k.p** interaction to the $\Gamma_6, \Gamma_7, \Gamma_8$ bands. This shortcoming can be solved by taking into account interaction between $\Gamma_6, \Gamma_7, \Gamma_8$ and remote bands only for the heavy particle states. The accuracy of the Kane model can be compared, for example, with the empirical tight-binding method, whose calculations are valid over whole Brillouin zone. The Kane model and global band structure descriptions coincide well for energies of the whole GaAs and AlAs bandgaps.

The knowledge of the value of P in III-V materials listed in Table 2.2 is instructive for the usage of Kane model. We notice that P is merely material independent. This result means that the rapidly varying function $u_{n\mathbf{k}}(\mathbf{r})$ of Bloch functions of the host band edges are quite similar in different materials.

Chapter 3

Band structure of heterostructures

3.1 Envelope function model

Advanced epitaxial techniques, such as molecular beam epitaxy or metal -organic chemical vapour deposition, have made it possible to grow interfaces between two semiconductors which are flat up to one atomic monolayer (2.83 Å in GaAs). The interface is usually represented as a continuously varying position-dependent band edge, assuming perfect bi-dimensional growth. Typical band edges for GaAs(material A)/GaAlAs(material B) profiles are shown in Fig. 3.1
We assume that the materials constituting the heterostructure are perfectly lattice-matched and have the same crystallographic structure. These assumptions are well justified for GaAs/GaAlAs. We make two assumptions:

- The wave function is expanded inside each layer to the periodic parts of the Bloch functions:
$$\Psi(\mathbf{r}) = \sum_l f_l^{(A)}(\mathbf{r}) u_{l,\mathbf{k_0}}^{(A)}(\mathbf{r}), \tag{3.1}$$

  if $\mathbf{r}$ corresponds to an A layer and

$$\Psi(\mathbf{r}) = \sum_l f_l^{(B)}(\mathbf{r}) u_{l,\mathbf{k_0}}^{(B)}(\mathbf{r}), \tag{3.2}$$

  if $\mathbf{r}$ corresponds to a B layer. $\mathbf{k_0}$ is the point in the Brillouin zone which the heterostructure states are built around. The summation runs over all edges included in the analysis.

- The periodic parts of the Bloch functions are assumed to be the same in each kind of layer which constitutes the heterostructure:
$$u_{l,\mathbf{k_0}}^{(A)}(\mathbf{r}) \equiv u_{l,\mathbf{k_0}}^{(B)}(\mathbf{r}) \equiv u_{l,\mathbf{k_0}}(\mathbf{r}) \tag{3.3}$$
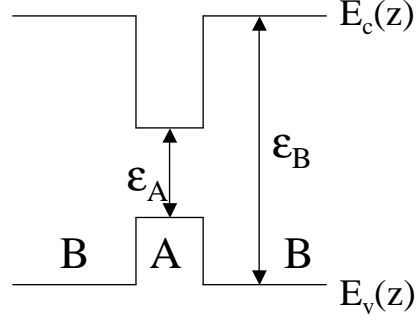
Figure 3.1: Conduction and valence band profiles.

Our truncation of the summation over l to a finite number of the band edges means that the actual dispersion relation of the host is well described by approximate energies $\varepsilon_l^{(A)}(\mathbf{k_A})$, $\varepsilon_l^{(B)}(\mathbf{k_B})$. According to the previous chapter we know that the conduction band states are well reproduced by the Kane model in both GaAs and AlAs.

Since the lattice constants of the host layers are assumed to be the same, the heterostructure becomes translationally invariant in the layer plane and f_l can thus be factorized into:

$$f_l^{A,B}(r_\perp, z) = \frac{1}{\sqrt{S}} \exp(i\mathbf{k}_\perp.\mathbf{r}_\perp)\chi_l^{A,B}(z), \tag{3.4}$$

where S is a sample area and $\mathbf{k}_\perp = (k_x, k_y)$ is a bi-dimensional wave vector, which is the same in both materials. Thus the heterostructure wave function is a sum of the product of rapidly varying functions $u_{l,\mathbf{k_0}}$ by slowly varying envelope function f_l. Hamiltonian takes form of:

$$H = \frac{p^2}{2m_0} + V_A(\mathbf{r})\theta_A + V_B(\mathbf{r})\theta_B, \tag{3.5}$$

where θ_A (θ_B) is a step function, unity in A (B) and zero in B (A).

Let H act upon $\Psi(\mathbf{r})$. Multiplying by $u_{m0}^*(\mathbf{r})\exp(i\mathbf{k}_\perp.\mathbf{r}_\perp)\chi_m^{*(A,B)}(z)$ and integrating over space we find after some computation that $\chi_l^{(A,B)}(z)$ fulfil a set of eigenvalue equations:

$$\mathbf{D^0}(z, -i\hbar\frac{\partial}{\partial z})\chi = \varepsilon\chi. \tag{3.6}$$

$\mathbf{D^0}$ is a matrix $N \times N$, where N is the number of band edges retained in eq. (3.1), (3.2):

$$D_{lm}^0(z, -i\hbar\frac{\partial}{\partial z}) = \left[\varepsilon_{l,0}^A\theta_A + \varepsilon_{l,0}^B\theta_B + \frac{\hbar^2 k_\perp^2}{2m_0} - \frac{\hbar^2}{2m_0}\frac{\partial^2}{\partial z^2}\right]\delta_{l,m} +$$
$$+ \frac{\hbar\mathbf{k}_\perp}{m_0}.\langle l|\mathbf{p}_\perp|m\rangle - \frac{i\hbar}{m_0}\langle l|p_z|m\rangle \cdot \frac{\partial}{\partial z}, \tag{3.7}$$

where:

$$\langle l|\mathbf{p}|m\rangle = \int_{\Omega_0} u_{l\mathbf{0}}^* \mathbf{p} u_{m\mathbf{0}} d^3 r \tag{3.8}$$

and Ω_0 is the unit cell of the host layer. In eq. (3.7) the larger N the more accurate the results will be. In practice we restrict N to 8, which means we study the heterostructure states attached to the $\Gamma_6, \Gamma_7, \Gamma_8$ bands of the host material. The effect of the remote bands can be taken into account only up to the second order in $\mathbf{p}$:

$$\left(\mathbf{D^0} - \frac{\hbar^2}{2} \sum_{\alpha,\beta} \frac{\partial}{\partial r_\alpha} \frac{1}{M^{\alpha\beta}} \frac{\partial}{\partial r_\beta} \right) \chi = \varepsilon\chi, \tag{3.9}$$

where:

$$\frac{m_0}{M_{lm}^{\alpha\beta}} = \frac{2}{m_0} \sum_\nu \langle l|p_\alpha|\nu\rangle \frac{1}{\bar{\varepsilon} - \varepsilon_{\nu 0}^{(A)} - \varepsilon_\nu^{(B)} + \varepsilon_\nu^{(A)}} \langle l|p_\beta|\nu\rangle. \tag{3.10}$$

As can be seen from eq. (3.7), (3.9), (3.10) the microscopic details of the heterostructure have explicitly disappeared being substituted by effective parameters: interband matrix elements, effective masses and band offset. To obtain boundary conditions we must integrate eq. (3.9) across the interface and as asymptotic behaviour we take that χ tends to zero at large z.

3.2 Ben Daniel-Duke model

The Ben Daniel-Duke model, which is the simplest one, works qualitatively for the lowest conduction states of GaAs/GaAlAs heterostructures with GaAs layer thickness larger than ~ 100 Å and for the heavy hole levels at $\mathbf{k}_\perp = \mathbf{0}$ in any heterostructure. We consider now a parabolic isotropic conduction band and effective masses m_A, m_B. Afterwards eq. (3.9) can be simplified to:

$$\left[\varepsilon_s + V_s(z) - \frac{\partial}{\partial z} \frac{1}{\mu(z)} \frac{\partial}{\partial z} + \frac{\hbar^2 k_\perp^2}{2\mu(z)} \right] \chi(z) = \varepsilon\chi(z) \tag{3.11}$$

$$\frac{1}{\mu(z)} = \frac{1}{m_0} + \frac{1}{M_{ss}^{zz}} \tag{3.12}$$

$$\mu(z) = \begin{cases} m_A & \text{in A layer} \\ m_B & \text{in B layer} \end{cases} \tag{3.13}$$

$$V_s(z) = \begin{cases} 0 & \text{in A layer} \\ V_s & \text{in B layer} \end{cases} \tag{3.14}$$

where V_s is the energy shift of the S band edge when going from the A to the B material. The boundary conditions simplify to the fact that $\chi(z)$, $\frac{1}{\mu(z)}\frac{d}{dz}$ are both continuous. If we study a quantum well schematized in Fig. 3.2 assuming $m_A, m_B > 0$ and taking
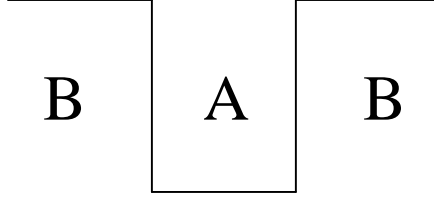
Figure 3.2: Quantum well.

into account that the potential is an even function we can write even solution:

$$\chi_{even}(z) \; = \; A\cos(k_A z) \qquad |z| \leq \frac{L_A}{2} \tag{3.15}$$

$$\chi_{even}(z) \; = \; B\exp\left[-\kappa_B(z - \frac{L_A}{2})\right] \qquad |z| \geq \frac{L_A}{2} \tag{3.16}$$

and odd solution:

$$\chi_{odd}(z) \; = \; A\sin(k_A z) \qquad |z| \leq \frac{L_A}{2} \tag{3.17}$$

$$\chi_{odd}(z) \; = \; B\exp\left[-\kappa_B(z - \frac{L_A}{2})\right] \qquad |z| \geq \frac{L_A}{2} \tag{3.18}$$

with:

$$\varepsilon - \varepsilon_s = \frac{\hbar^2 k_A^2}{2m_A} + \frac{\hbar^2 k_\perp^2}{2m_A} = V_s - \frac{\hbar^2 \kappa_B^2}{2m_B} - \frac{\hbar^2 \kappa_\perp^2}{2m_B}. \tag{3.19}$$

By matching boundary conditions we get:

$$\cos(\varphi_A) - \frac{m_A}{m_B}\frac{k_A}{\kappa_B}\sin(\varphi_A) \; = \; 0 \qquad \text{for even states} \tag{3.20}$$

$$\cos(\varphi_A) + \frac{m_A}{m_B}\frac{\kappa_B}{k_A}\sin(\varphi_A) \; = \; 0 \qquad \text{for odd states} \tag{3.21}$$

$$\varphi_A \; = \; \frac{1}{2}k_A L_A. \tag{3.22}$$

Two interesting cases are shown in Fig. 3.3. When $m_A - m_B$ is small enough we can rewrite eq. (3.11) using:

$$\frac{\hbar^2 k_\perp^2}{2\mu(z)} = \frac{\hbar^2 k_\perp^2}{2m_n} + \frac{\hbar^2 k_\perp^2}{2}\left[\frac{1}{\mu(z)} - \frac{1}{m_n}\right] \tag{3.23}$$

and taking the second term as a perturbation to $\mathcal{H}'$

$$\mathcal{H}' = \varepsilon_s + V_s(z) - \frac{\partial}{\partial z}\frac{1}{\mu(z)}\frac{\partial}{\partial z} + \frac{\hbar^2 k_\perp^2}{2m_n}. \tag{3.24}$$
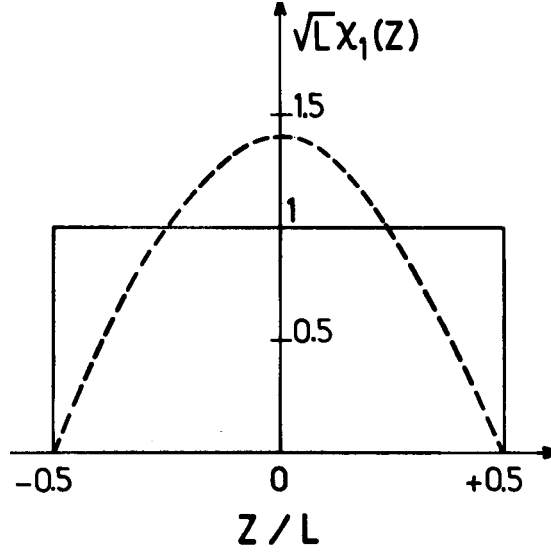
Figure 3.3: Ground state envelope functions for a quantum well with infinite V_s (dashed line) or with finite V_s but infinite $\frac{m_B}{m_A}$ (solid line), taken from [9].

The first order corrections to the unperturbated eigenstates are then given by:

$$\Delta E_n = \frac{\hbar^2 k_\perp^2}{2} \left[\frac{1}{m_A}[1 - P_b(E_n)] + \frac{1}{m_b} P_b(E_n) - \frac{1}{m_n} \right], \qquad (3.25)$$

where:

$$P_b(E_n) = 2 \int_{\frac{L_A}{2}}^{\infty} \chi_n^2(z) dz \qquad (3.26)$$

is the integrated probability of finding the electron in the barriers while in the nth state. The dispersion relation takes form of:

$$E_n(k_\perp) \simeq \varepsilon_s + E_n(0) + \frac{\hbar^2 k_\perp^2}{2m_n}. \qquad (3.27)$$

With this equation we can easily compute the density of states defined as:

$$\rho(\varepsilon) = \sum_\nu \delta(\varepsilon - \varepsilon_\nu), \qquad (3.28)$$

where ε_ν is the energy associated with the state $|\nu\rangle$. The density of states gives us information about how many states $|\nu\rangle$ per unit energy are available around a given
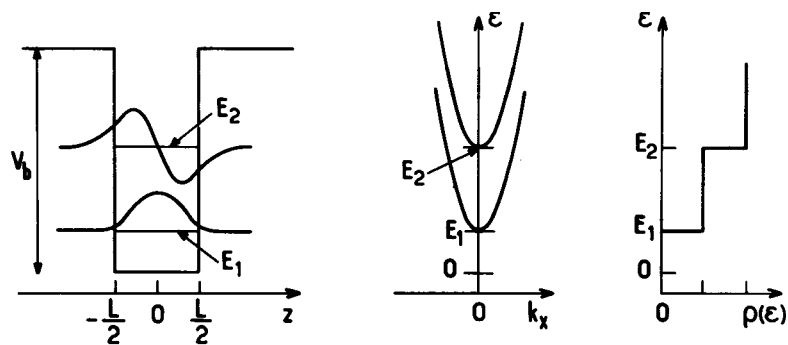
Figure 3.4: Properties of the solution of eq. (3.24), taken from [9].

energy ε. We obtain after some manipulation:

$$\rho(\varepsilon) = \sum_n \rho_n(\varepsilon) \tag{3.29}$$

$$\rho_n(\varepsilon) = \frac{m_n}{\pi\hbar^2}\theta(\varepsilon - E_n), \tag{3.30}$$

where $\theta(x)$ is a step function. The properties of the solution are summarized in Fig. 3.4.

Chapter 4

Excitons

4.1 Excitons in idealized bulk materials

We consider a bulk material with a single spherical conduction band with a dispersion relation:

$$\varepsilon_c(\mathbf{k}) = \varepsilon_g + \frac{\hbar^2 k^2}{2m_c^*},$$ (4.1)

which is separated by energy ε_g from the valence band with a dispersion relation:

$$\varepsilon_v(\mathbf{k}) = \frac{-\hbar^2 k^2}{2m_v^*}.$$ (4.2)

The ground state of a semiconductor is a state with valence band filled by electrons and empty conduction band. When promoting an electron with $\mathbf{k_c}$ from the valence band to the conduction band the hole with $\mathbf{k_h} = -\mathbf{k_v}$ and m_v^* appears. Neglecting the Coulomb interaction the energy of the first excited state is ε_g. Taking into account the Coulomb interaction the energy of the excited state can be lowered as can be seen from the solution of the following equation:

$$\left[\frac{p_e^2}{2m_c^*} + \frac{p_h^2}{2m_v^*} - \frac{e^2}{\kappa |\mathbf{r_e} - \mathbf{r_h}|} \right] \Psi(\mathbf{r_e}, \mathbf{r_h}) = (\varepsilon - \varepsilon_g)\Psi(\mathbf{r_e}, \mathbf{r_h}).$$ (4.3)

This Hamiltonian has the same structure as the Hamiltonian of the hydrogen atom and it can be solved in the same way. We define new coordinates, centre-of-mass and relative distance of the electron-hole pair:

$$\mathbf{r} = \mathbf{r_e} - \mathbf{r_h}$$ (4.4)

$$\mathbf{R} = \frac{m_c^* \mathbf{r_e} + m_v^* \mathbf{r_h}}{m_c^* + m_v^*}.$$ (4.5)

We can thus rewrite eq. (4.3) in the following form

$$\left[\frac{P_e^2}{2m_c^* + 2m_v^*} + \frac{p^2}{2\mu} - \frac{e^2}{\kappa r}\right]\Psi(\mathbf{r}, \mathbf{R}) = (\varepsilon - \varepsilon_g)\Psi(\mathbf{r}, \mathbf{R}), \tag{4.6}$$

where:

$$\mathbf{P} = -i\hbar\frac{\partial}{\partial\mathbf{R}} \tag{4.7}$$

$$\mathbf{p} = -i\hbar\frac{\partial}{\partial\mathbf{r}} \tag{4.8}$$

$$\mu = \frac{m_c^* m_v^*}{m_c^* + m_v^*}. \tag{4.9}$$

Solution of eq. (4.6) can be written as:

$$\Psi(\mathbf{r}, \mathbf{R}) = \frac{1}{\sqrt{\Omega}}\exp(i\mathbf{K}\mathbf{R})\varphi(\mathbf{r}), \tag{4.10}$$

Ω being the crystal volume and $\varphi(\mathbf{r})$ satisfying the equation:

$$\left[\frac{p^2}{2\mu} - \frac{e^2}{\kappa r}\right]\varphi(\mathbf{r}) = \xi\varphi(\mathbf{r}). \tag{4.11}$$

The total energy can be expressed as:

$$\varepsilon = \varepsilon_g + \xi + \frac{\hbar^2 K^2}{2(m_c^* + m_v^*)}. \tag{4.12}$$

For the ground state the energy and wave function are equal to:

$$\xi = -\frac{\mu e^4}{2\kappa^2\hbar^2} \tag{4.13}$$

$$\varphi(\mathbf{r}) = \frac{1}{\sqrt{\pi a_0^3}}\exp(-r/a_0), \tag{4.14}$$

where

$$a_0 = \frac{\hbar^2\kappa}{\mu e^2} \tag{4.15}$$

is the effective radius. We can interpret this solution as the motion of a fictitious particle with mass $M = m_c^* + m_v^*$ and with kinetic energy $\frac{\hbar^2 K^2}{2M}$. This particle is called exciton and consists of an electron and a hole which orbit around each other and whose centre-of-mass moves.

4.2   Excitons in idealized well structures

Let us consider a slab of material A between two layers of material B. Assuming the same dielectric constants κ, the same effective masses m_c^*, m_v^* of the conduction and valence band respectively in both materials and supposing that material A confines both electrons and holes, we write the Hamiltonian:

$$\mathcal{H} = \frac{p_e^2}{2m_c^*} + \frac{p_h^2}{2m_v^*} - \frac{e^2}{\kappa|\mathbf{r_e} - \mathbf{r_h}|} + V_e + V_h, \tag{4.16}$$

where V_e, V_h are step like potentials for the electron (hole) in the z direction. We can use the same procedure as in the previous section to separate the relative and centre-of-mass motion, but in this case it is only possible to do so in the x and y direction. We introduce the vectors $\mathbf{R}_\perp, \rho$:

$$\rho = \rho_\mathbf{e} - \rho_\mathbf{h} \tag{4.17}$$

$$\mathbf{R}_\perp = \frac{m_e\rho_\mathbf{e} + m_h\rho_\mathbf{h}}{m_e + m_h}, \tag{4.18}$$

where we have changed the notation $m_{c(v)}^* = m_{e(h)}$. And finally we obtain:

$$\mathcal{H} = \frac{P_e^2}{2m_e + 2m_h} + \frac{p^2}{2\mu} - \frac{e^2}{\kappa\sqrt{\rho^2 + (z_e - z_h)^2}} + \frac{p_{ze}^2}{2m_e} + \frac{p_{zh}^2}{2m_h} + V_e + V_h + \varepsilon_g, \tag{4.19}$$

which leads to the factorization of the wave function:

$$\Psi(\mathbf{r_e}, \mathbf{r_e}) = \frac{1}{\sqrt{S}} \exp(i\mathbf{K}_\perp\mathbf{R}_\perp)\varphi(z_e, z_h, \rho). \tag{4.20}$$

In comparison with eq. (4.6) we have introduced a two-dimensional exciton in the xy plane. Since eq. (4.20) is quite similar to eq. (4.6) the common technique to solve this equation is using Gaussian sets or non linear variational parameters [12]. The latter technique was used to write the solution:

$$\varphi(z_e, z_h, \rho) = N\chi_e(z_e)\chi_h(z_h) \exp\left(\frac{-1}{\lambda}\sqrt{\rho^2 + (z_e - z_h)^2}\right), \tag{4.21}$$

where N is a normalization constant and λ is a variational parameter. The electrons in the lowest conduction band and the holes in the lowest hole band were considered. We should note that there are two kinds of excitons: those with heavy holes called heavy hole excitons and those with light holes called light hole excitons. The light hole excitons are always less bound than the heavy hole excitons.
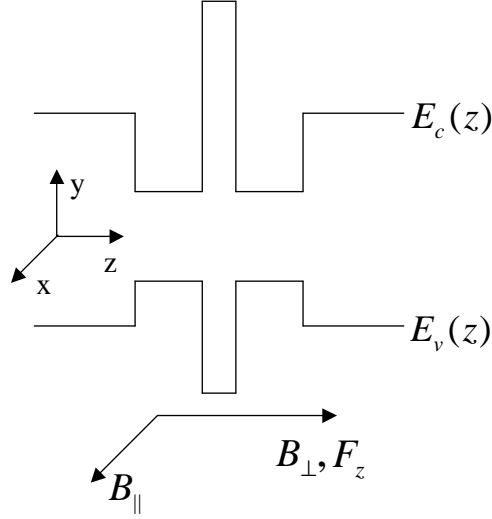
Figure 4.1: Double quantum well in electric and magnetic field.

4.3 Excitons in idealized double quantum well

4.3.1 Introduction

In this section we will deal with excitons in the double quantum well (DQW) in electric and magnetic field. The situation is shown in Fig. 4.1. The problem of the exciton in DQW in the electric field is solved in [2] by variational method. We will use a different approach but some result of [2] will also be useful to us. The theory is taken from the major part from [5]. We define a direct (indirect) exciton as an exciton composed of an electron and a hole found in a same (different) well.

4.3.2 Tight-binding basis

The electron (hole) in the magnetic **B** and electric field **F** is described by the Hamiltonian:

$$H_{e(h)} = \frac{1}{m_{e(h)}} \left[\mathbf{p}_{e(h)} \pm e\mathbf{A}_{e(h)} \right]^2 + V_{e(h)}(z_{e(h)}) \pm e\mathbf{r}_{e(h)}\mathbf{F}, \qquad (4.22)$$

where $V_{e(h)}(z_{e(h)})$ are step like functions of the double well potential for the electron (hole). In our approach the electric field will be non zero only in the z direction and will thus model the asymmetry of the symmetrical DQW:

$$\mathbf{F} = e_z F, \qquad (4.23)$$

where e_z is a unity vector in the z direction. First we discuss the magnetic field in the x direction (parallel to the xy plane). Our choice of the gauge for the vector potential

A is:

$$\mathbf{A}(\mathbf{r}) = -B_{\parallel}ze_y. \tag{4.24}$$

The next step is the introduction of the magnetic field dependent tight-binding basis function $|e(h), j\rangle$ (j=1,2 is quantum well number)

$$|e(h), j\rangle = \varphi_{e(h)}^j(z_{e(h)}) \exp\left(\mp iz_j y_{e(h)} \frac{eB_{\parallel}}{\hbar}\right), \tag{4.25}$$

where $\varphi_{e(h)}^j(z_{e(h)})$ is the tight-binding basis function describing an electron (hole) in the jth well in the absence of external field. Such a choice of the basis functions assumes that the size quantization energy is the largest energy scale and the relation

$$\Delta E_n \gg \hbar\omega_0, \tag{4.26}$$

is satisfied. ΔE_n represents the energy separation between size-quantized levels in each well and $\omega_0 = eB/m$ is the cyclotron frequency. The z_j is the coordinate of the jth QW centre. We introduce the energy in z direction and tunnelling elements:

$$\varepsilon_{e(h)}(B) = \langle\varphi_{e(h)}^{1(2)}(z_{e(h)})|V_{e(h)} + \frac{p_z^2}{2m_{e(h)}} + \frac{e^2B_{\parallel}^2}{2m_{e(h)}}(z_{e(h)} - z_{1(2)e(h)})^2|\varphi_{e(h)}^{1(2)}(z_{e(h)})\rangle \tag{4.27}$$

$$t_{e(h)} = \langle\varphi_{e(h)}^{1(2)}(z_{e(h)})|V_{e(h)} + \frac{p_z^2}{2m_{e(h)}} + \frac{e^2B_{\parallel}^2}{2m_{e(h)}}(z - z_{2(1)})^2|\varphi_{e(h)}^{2(1)}(z_{e(h)})\rangle. \tag{4.28}$$

The last term in eq. (4.27) is a usual diamagnetic shift. We neglect the same term in eq. (4.28) (as basis function are almost orthogonal) and shall consider the tunnelling element $t_{e(h)}$ being field independent in our approximation. We also neglect the intrawell Stark effect which does not change the qualitative results. The Hamiltonian in this basis then takes form of a 2×2 matrix with elements:

$$H_{e(h)}^{11(22)} = \langle e, 1(2)|H|e, 1(2)\rangle = \varepsilon_{e(h)}(B) + \frac{\mathbf{p}_{\parallel}^2}{2m_{e(h)}} \pm (\mp)edF \tag{4.29}$$

$$H_{e(h)}^{12(21)} = \langle e, 1(2)|H|e, 2(1)\rangle = t_{e(h)}\exp\left(\pm(\mp)\frac{dy_{e(h)}eB_{\parallel}}{\hbar}\right), \tag{4.30}$$

where d is the interwell distance.

4.3.3   Electron-hole interaction

After introducing the tight-binding basis we write the initial electron-hole two-particle Hamiltonian in the effective mass approximation

$$H = \frac{1}{m_e}(\mathbf{p}_e + e\mathbf{A_e})^2 + V_e(z_e) + \frac{1}{m_h}(\mathbf{p}_h - e\mathbf{A_h})^2 + V_h(z_h) + C(\mathbf{r}_e - \mathbf{r}_h), \tag{4.31}$$

where $C(\mathbf{r}_e - \mathbf{r}_h)$ is a potential describing the electron-hole interaction. We use either Coulomb potential for the numerical calculations or quadratic potential for the analytical calculations. We also use two different gauges, symmetric for the analytical and numerical calculations:

$$\mathbf{A} = (-\frac{1}{2}B_\perp y, \frac{1}{2}B_\perp x - B_\| z, 0) \tag{4.32}$$

and asymmetric only for the numerical calculation to test the numerical precision and stability:

$$\mathbf{A} = (0, B_\perp x - B_\| z, 0). \tag{4.33}$$

We introduce the "two-particle" tight-binding basis with the following four basis functions

$$|i, j\rangle = |e, i\rangle |h, j\rangle \tag{4.34}$$

to describe excitonic effects. Using eq. (4.25) we can write this basis explicitly

$$
\begin{aligned}
|1, 1\rangle &= \varphi_e^1(z_e)\varphi_h^1(z_h) \exp\left[-iz_1(y_e - y_h)\frac{eB_\|}{\hbar}\right] \\
|1, 2\rangle &= \varphi_e^1(z_e)\varphi_h^2(z_h) \exp\left[-i(z_1 y_e - z_2 y_h)\frac{eB_\|}{\hbar}\right] \\
|2, 1\rangle &= \varphi_e^2(z_e)\varphi_h^1(z_h) \exp\left[-i(z_2 y_e - z_1 y_h)\frac{eB_\|}{\hbar}\right] \\
|2, 2\rangle &= \varphi_e^2(z_e)\varphi_h^2(z_h) \exp\left[-iz_2(y_e - y_h)\frac{eB_\|}{\hbar}\right].
\end{aligned}
\tag{4.35}
$$

The introduction of the basis in eq. (4.34) enables us to separate z and parallel (with respect to the xy plane) motion and to derive the matrix Schrödinger equation for the wave functions depending only on the transverse coordinates $\mathbf{r}_{e(h)}$. Thus projecting Hamiltonian from eq. (4.31) on the basis eq. (4.34) we obtain the following system of equations

$$
\begin{aligned}
\left(\hat{H} - C_{11} + \Delta\right)\chi_{11} - t_h \exp(-i\frac{dy_h eB_\|}{\hbar})\chi_{12} - t_e \exp(i\frac{dy_e eB_\|}{\hbar})\chi_{21} &= \varepsilon\chi_{11} \\
\left(\hat{H} - C_{12} + \Delta\right)\chi_{12} - t_h \exp(i\frac{dy_h eB_\|}{\hbar})\chi_{11} - t_e \exp(i\frac{dy_e eB_\|}{\hbar})\chi_{22} &= \varepsilon\chi_{12} \\
\left(\hat{H} - C_{21} + \Delta\right)\chi_{21} - t_e \exp(-i\frac{dy_e eB_\|}{\hbar})\chi_{11} - t_h \exp(-i\frac{dy_h eB_\|}{\hbar})\chi_{22} &= \varepsilon\chi_{21} \\
\left(\hat{H} - C_{22} + \Delta\right)\chi_{22} - t_h \exp(i\frac{dy_h eB_\|}{\hbar})\chi_{21} - t_e \exp(-i\frac{dy_e eB_\|}{\hbar})\chi_{12} &= \varepsilon\chi_{22}, \quad (4.36)
\end{aligned}
$$

where

$$\Delta = \varepsilon_e(B) + \varepsilon_h(B) \tag{4.37}$$

and we assume that the electrons and holes are in the ground state in z direction. The elements of $\mathbf{C}$ are expressed by:

$$C_{ij} = \int dz_e dz_h \varphi_i^2(z_e) C(r_e - r_h) \varphi_j^2(z_h). \tag{4.38}$$

The operator $\hat{H}$ is defined as:

$$\hat{H} = \frac{\hat{\mathbf{P}}_e^2}{m_e} + \frac{\hat{\mathbf{P}}_h^2}{m_h} \tag{4.39}$$

$$\hat{\mathbf{P}}_{e(h)} = \mathbf{p}_{e(h),\parallel} \pm \frac{1}{2}(e_z \times \mathbf{r}_{e(h)}) e B_\perp. \tag{4.40}$$

4.3.4 Excitonic centre-of-mass separation

In the next step, which is the centre-of-mass separation, we use a procedure similar to the one proposed in [13] and generalize it to the case of a multicomponent wave function. We look for the solution of the system of equations (4.36) in the following form:

$$\begin{pmatrix} \chi_{11} \\ \chi_{12} \\ \chi_{21} \\ \chi_{22} \end{pmatrix} = \exp\left[(K_x - \frac{eB_\perp}{2\hbar}y)X + (K_y + \frac{eB_\perp}{2\hbar}x)Y\right] \begin{pmatrix} u_{11}(r) \\ u_{12}(r)\exp\left(i\frac{dYeB_\parallel}{\hbar}\right) \\ u_{21}(r)\exp\left(-i\frac{dYeB_\parallel}{\hbar}\right) \\ u_{22}(r) \end{pmatrix}, \tag{4.41}$$

where the centre-of-mass coordinate is equal to

$$\mathbf{R} = \frac{m_e \mathbf{r}_e + m_h \mathbf{r}_h}{m_e + m_h} \tag{4.42}$$

and the coordinate of the relative motion is expressed by

$$\mathbf{r} = \mathbf{r}_e - \mathbf{r}_h. \tag{4.43}$$

Introducing eq. (4.41) in eq. (4.36) we get the following Hamiltonian for the basis (4.41):

$$H = \begin{pmatrix} \hat{h}_{11}(\hat{\mathbf{k}}, \mathbf{K}, \mathbf{r}) & T_h(y) & T_e(y) & 0 \\ T_h^*(y) & \hat{h}_{12}(\hat{\mathbf{k}}, \mathbf{K} - e_y\frac{deB_\parallel}{\hbar}, \mathbf{r}) & 0 & T_e^*(y) \\ T_e^*(y) & 0 & \hat{h}_{21}(\hat{\mathbf{k}}, \mathbf{K} + e_y\frac{deB_\parallel}{\hbar}, \mathbf{r}) & T_h^*(y) \\ 0 & T_e(y) & T_h(y) & \hat{h}_{22}(\hat{\mathbf{k}}, \mathbf{K}, \mathbf{r}) \end{pmatrix}, \tag{4.44}$$

where

$$\hat{h}_{ij}(\hat{\mathbf{k}}, \mathbf{K}, \mathbf{r}) = \hat{h}(\hat{\mathbf{k}}, \mathbf{K}, \mathbf{r}) - C_{ij} \tag{4.45}$$

$$\hat{h}(\hat{\mathbf{k}}, \mathbf{K}, \mathbf{r}) = \frac{\hbar^2}{2} \frac{K_x^2 + K_y^2}{M} + \frac{\hat{\mathbf{k}}^2}{2m} + \frac{eB_\perp \hbar}{M}(K_y x - K_x y) + \tag{4.46}$$
$$+ \frac{e^2 B_\perp^2}{8m}(x^2 + y^2) - \frac{\gamma e B_\perp \hbar}{2m}(x\hat{k}_y - y\hat{k}_x),$$

which can be rewritten:

$$\hat{h}(\hat{\mathbf{k}}, \mathbf{K}, \mathbf{r}) = \frac{\hat{\mathbf{k}}^2}{2m} - \frac{\gamma e B_\perp \hbar}{2m}(e_z \times \mathbf{r})\hat{\mathbf{k}} + \frac{e^2 B_\perp^2}{8m}(e_z \times \mathbf{r})^2 + \frac{eB_\perp \hbar}{M}(e_z \times \mathbf{r})\mathbf{K} + \frac{\mathbf{K}^2}{2M}, \tag{4.47}$$

where $\mathbf{K}$ is the centre-of-mass momentum, $\hat{\mathbf{k}} = -i\hbar\frac{\partial}{\partial \mathbf{r}}$ is the relative motion momentum, M is the total mass of the exciton, $m = m_e m_h / M$ is the reduced mass and $\gamma = (m_e - m_h)/M$. If $B_\parallel$ is non zero then the tunnelling matrix elements acquire a phase factor and become functions of the coordinate y:

$$T_{e(h)}(y) = t_{e(h)} \exp(i\frac{dy e B_\parallel}{\hbar} \frac{m_{h(e)}}{M}). \tag{4.48}$$

We can make an important conclusion from the structure of the Hamiltonian in eq. (4.44). Under the condition $B_\parallel \neq 0$ the excitons indirect in r-space become also indirect in k-space, thus their energy minimum shifts by $\delta\mathbf{K} = e_y\frac{deB_\parallel}{\hbar}$ from zero. This momentum shift results from the correspondence between the centre of the orbit of the charged particle in the magnetic field $B_\parallel$ and the y-component of the momentum. Thus electron and hole separated in real space by the distance d are separated by the vector $e_y\frac{deB_\parallel}{\hbar}$ in the momentum space.

4.3.5   Parabolic potential

To pursue the analytical solution of the Hamiltonian (4.44) as far as possible, we introduce a parabolic potential into eq. (4.45) and phenomenological constants in order to describe the energy separation of the direct (d) and indirect (ind) exciton levels:

$$C_{11,22} = C_d r^2 - S_d \tag{4.49}$$
$$C_{12,21} = C_{ind} r^2 - S_{ind}. \tag{4.50}$$

First we find eigenvalues and wave functions of the diagonal elements of the matrix (4.44), that is to say we solve the Hamiltonian:

$$H_{(in)d} = \frac{\hat{\mathbf{k}}^2}{2m} - \frac{\gamma e B_\perp \hbar}{2m}(e_z \times \mathbf{r})\hat{\mathbf{k}} + \frac{e^2 B_\perp^2}{8m}(e_z \times \mathbf{r})^2 +$$
$$+ \frac{eB_\perp \hbar}{M}(e_z \times \mathbf{r})\mathbf{K} + \frac{\mathbf{K}^2}{2M} + C_{(in)d} r^2 - S_{(in)d}. \tag{4.51}$$

If $B_\perp = 0$ the solution are Hermit polynomials, we write the first wave function ($N_{(in)d}$ is a normalization constant)

$$\Phi_{(in)d}(r) = N_{(in)d} \exp\left(-r^2\sqrt{\frac{C_{(in)d}m}{2\hbar^2}}\right) \tag{4.52}$$

and energy levels

$$\varepsilon_{n_x,m_y}^{(in)d} = \sqrt{\frac{2C_{(in)d}\hbar^2}{m}}(n_x + m_y + 1) - S_{(in)d}, \tag{4.53}$$

where n_x, m_y are quantum numbers of the energy levels in the x, y direction. When $B_\perp \neq 0$ we can solve eq. (4.51) if we interpret the components with $(e_z \times \mathbf{r})\mathbf{K}$ as the shift of the centre of the potential and if we shift the magnetic field in the same way, in other words if we change the gauge, we get the wave function of the first energy level:

$$\Phi_{(in)d}(\mathbf{r}, \mathbf{K}) = N_{(in)d} \exp\left[-((x - G_{(in)d}(\mathbf{K})B_\perp)^2 + (y + F_{(in)d}(\mathbf{K})B_\perp)^2)D_{(in)d}\right]$$
$$\exp\left(i\frac{B_\perp^2}{2\hbar}(F_{(in)d}(\mathbf{K})x + G_{(in)d}(\mathbf{K})y)e\gamma\right), \tag{4.54}$$

where

$$D_{(in)d} = \frac{\sqrt{\frac{1}{16}e^2 B_\perp^2 + \frac{1}{2}C_{(in)d}m}}{\hbar} \tag{4.55}$$

$$F_{(in)d}(\mathbf{K}) = \frac{-4e\hbar K_x m}{M(e^2 B_\perp^2 + 8C_{(in)d}m - e^2\gamma^2 B_\perp^2)} \tag{4.56}$$

$$G_{(in)d}(\mathbf{K}) = \frac{-4e\hbar K_y m}{M(e^2 B_\perp^2 + 8C_{(in)d}m - e^2\gamma^2 B_\perp^2)} \tag{4.57}$$

and the energy of the first level is equal to:

$$E_{(in)d}(\mathbf{K}) = -S_{(in)d} + \frac{1}{8m}\left(4\sqrt{e^2 B^2 + 8C_{(in)d}m}B_\perp^2\hbar - \right.$$
$$\left. - (G_{(in)d}(\mathbf{K})^2 + F_{(in)d}(\mathbf{K})^2)(1 - \gamma^2)e^2 B_\perp^2 - 8(G_{(in)d}(\mathbf{K})^2 + F_{(in)d}(\mathbf{K})^2)C_{(in)d}\right)m. \tag{4.58}$$

We project the Hamiltonian (4.44) on the basis $\Phi_d(\mathbf{r})$, $\Phi_{ind}(\mathbf{r})$ and we switch the electric field on, which models the asymmetry of the DQW. And afterwards we get:

$$H = \begin{pmatrix} E_d(\mathbf{K}) & T_h & T_e & 0 \\ T_h^* & E_{ind}(\mathbf{K} - e_y\frac{deB_\parallel}{\hbar}) + ed\mathbf{F} & 0 & T_e^* \\ T_e^* & 0 & E_{ind}(\mathbf{K} + e_y\frac{deB_\parallel}{\hbar}) - ed\mathbf{F} & T_h^* \\ 0 & T_e & T_h & E_d(\mathbf{K}) \end{pmatrix}, \tag{4.59}$$

where

$$T_{e(h)} = t_{e(h)} \int \exp(i\frac{dyeB_{\parallel}}{\hbar}\frac{m_{h(e)}}{M})\Phi_d^*(\mathbf{r}, \mathbf{K})\Phi_{ind}(\mathbf{r}, \mathbf{K}). \tag{4.60}$$

The Hamiltonian (4.59) can be easily solved numerically in reasonable time. The question of setting the phenomenological parameters $S_{(in)d}, C_{(in)d}$ will be discussed later and we will show that this approach can give good agreement with the precise numerical calculations.

4.3.6   Expansion of the wave function

In this section we expand the wave function into a basis of eigenfunctions of the angular momentum in order to obtain the Hamiltonian in a convenient form for the numerical solution. We expand the coefficients of the tight-binding basis $(i, j = m)$ in this way:

$$\Upsilon^m(\mathbf{r}, \mathbf{K}) = \sum_{k=-\infty}^{+\infty} f_k^m(\mathbf{r}, \mathbf{K}) \exp(ik\phi). \tag{4.61}$$

If we act with the general Hamiltonian on this basis we get:

$$\sum_{m=1}^{4} \hat{H}_{nm}(r, \phi, \mathbf{K})\Upsilon^m(r, \phi, \mathbf{K}) = E(\mathbf{K})\Upsilon^n(r, \phi, \mathbf{K}) \tag{4.62}$$

$$\sum_{m=1}^{4} \hat{H}_{nm}(r, \phi, \mathbf{K}) \sum_{k=-\infty}^{+\infty} f_k^m(r, \mathbf{K}) \exp(ik\phi) = E(\mathbf{K}) \sum_{k=-\infty}^{+\infty} f_k^n(r, \mathbf{K}) \exp(ik\phi) \tag{4.63}$$

$$\sum_{m=1}^{4} \sum_{k=-\infty}^{+\infty} \exp(i(k-k_0)\phi)\hat{H}_{nm}^k(r, \phi, \mathbf{K})f_k^m(r, \mathbf{K}) = E(\mathbf{K}) \sum_{k=-\infty}^{+\infty} f_k^n(r, \mathbf{K}) \exp(i(k-k_0)\phi), \tag{4.64}$$

where

$$\hat{H}_{nm}^k(r, \phi, \mathbf{K}) = \exp(-ik\phi)\hat{H}_{nm}(r, \phi, \mathbf{K})\exp(ik\phi). \tag{4.65}$$

Afterwards we integrate eq. (4.64) to obtain an equation for each term of the expansion (4.61) which will be solved numerically:

$$\frac{1}{2\pi} \sum_{m=1}^{4} \sum_{k=-\infty}^{+\infty} \int_0^{2\pi} \hat{H}_{nm}^k(r, \phi, \mathbf{K}) \exp(i(k-k_0)\phi)d\phi f_k^m(r, \mathbf{K}) = E(\mathbf{K})f_{k_0}^n(r, \mathbf{K}) \tag{4.66}$$

and we shall denote

$$\frac{1}{2\pi} \sum_{k=-\infty}^{+\infty} \int_0^{2\pi} \hat{H}_{nm}^k(r, \phi, \mathbf{K}) \exp(i(k-k_0)\phi)d\phi f_k^m(r, \mathbf{K}) \equiv \hat{H}_{nm}^{k_0}(r, \mathbf{K})f_k^m(r, \mathbf{K}). \tag{4.67}$$

We compute the matrix elements $H_{nm}^k(r, \mathbf{K})$ for the Hamiltonian (4.44) and we start with the diagonal elements described in eq. (4.45). First we write polar coordinates and their derivatives:

$$
\begin{align}
x &= r \cos \phi \tag{4.68} \\
y &= r \sin \phi \tag{4.69} \\
\frac{\partial}{\partial x} &= \cos \phi \frac{\partial}{\partial r} - \frac{1}{r} \sin \phi \frac{\partial}{\partial \phi} \tag{4.70} \\
\frac{\partial}{\partial y} &= \sin \phi \frac{\partial}{\partial r} + \frac{1}{r} \cos \phi \frac{\partial}{\partial \phi} \tag{4.71} \\
\Delta_\perp &= \frac{\partial^2}{\partial r^2} + \frac{1}{r} \frac{\partial}{\partial r} + \frac{1}{r^2} \frac{\partial^2}{\partial \phi^2}. \tag{4.72}
\end{align}
$$

Substituting these derivatives into eq. (4.47) we get:

$$
\hat{H}_{ii}(\mathbf{K}) = \frac{1}{2m} \Delta_\perp + i \frac{\gamma e B_\perp \hbar}{2m} \frac{\partial}{\partial \phi} + \frac{e^2 B_\perp^2}{8m} r^2 + \frac{e B_\perp \hbar}{M} (K_y r \cos \phi - K_x r \sin \phi) + \frac{\mathbf{K^2}}{2M} \tag{4.73}
$$

and following the procedure for getting $H_{nm}^k(r, \mathbf{K})$ we can write

$$
\hat{H}_{ii}^{k_0}(\mathbf{K}) = \frac{1}{2m} \left(\frac{\partial^2}{\partial r^2} + \frac{1}{r} \frac{\partial}{\partial r} - \frac{k^2}{r^2} \right) \delta_{k,k_0} - \frac{\gamma e B_\perp \hbar}{2m} k \delta_{k,k_0} +
$$

$$
+ \frac{e^2 B_\perp^2}{8m} r^2 \delta_{k,k_0} + \frac{e B_\perp \hbar}{2M} (K_y r (\delta_{k,k_0+1} + \delta_{k,k_0-1}) - i K_x (\delta_{k,k_0+1} - \delta_{k,k_0-1})) + \frac{\mathbf{K^2}}{2M} \delta_{k,k_0} \tag{4.74}
$$

By the same way we obtain the off-diagonal matrix elements

$$
\hat{H}_{ij}^{k_0} = t_{e(h)} \frac{1}{2\pi} \sum_{k=-\infty}^{+\infty} \int_0^{2\pi} \exp \left(ir \sin \phi \frac{e d B_\perp}{\hbar} \frac{m_{h(e)}}{M} + i(k - k_0)\phi \right) d\phi. \tag{4.75}
$$

Using the identities for the Bessel functions [14]:

$$
\begin{align}
J_n(x) &= \frac{1}{2\pi} \int_0^{2\pi} \exp[i(x \sin \phi - n\phi)] d\phi \tag{4.76} \\
J_n(x) &= J_{-n}(x) \text{ n even} \tag{4.77} \\
J_n(x) &= -J_{-n}(x) \text{ n odd} \tag{4.78}
\end{align}
$$

we can write

$$
\hat{H}_{ij}^{k_0} = \sum_{k=-\infty}^{+\infty} t_{e(h)} J_n \left(r \frac{e d B_\perp}{\hbar} \frac{m_{h(e)}}{M} \right) \delta_{k-n,k_0}. \tag{4.79}
$$

Now we can proceed to numerical calculations, which is the topic of the chapter 5.

4.3.7 Dependence of the energy on K_x

In this section we show why a dependence of the energy on K_x will not be of our main interest. We shall write an equation for an exciton in simple quantum well (using eq. (4.45)

$$\left(\hat{h}(\hat{\mathbf{k}}, \mathbf{K}, \mathbf{r}) - C_{ij}(\mathbf{r})\right)\Phi_{ij}(\mathbf{r}) = E_{ij}(\mathbf{K})\Phi_{ij}(\mathbf{r}). \qquad (4.80)$$

Introducing the transformation

$$\Phi_{ij}(\mathbf{r}) = \exp\left(-\frac{1}{2}i\gamma\mathbf{r}\mathbf{K}\right)\Psi_{ij}(\mathbf{r} - \mathbf{r_0}) \qquad (4.81)$$

$$\mathbf{r_0} = \frac{\hbar}{eB_\perp}(-K_y, K_x) \qquad (4.82)$$

we rewrite (4.80)

$$\left(\hat{h}(\hat{\mathbf{k}}, \mathbf{0}, \mathbf{r}) - C_{ij}(\mathbf{r} + \mathbf{r_0})\right)\Psi_{ij}(\mathbf{r}) = E_{ij}(\mathbf{K})\Psi_{ij}(\mathbf{r}). \qquad (4.83)$$

We know from the symmetry of the problem that $E_{ij}(\mathbf{K})$ is an even function of $\mathbf{K}$. We also know from the structure of eq. (4.83) that the dependence of the energy on K_x is monotone since K_x only shifts the centre of the potential from the origin and there is no reason for any local extremum. This can be understood if we realize the analogy with harmonic oscillator where the shift of the potential doesn't change the energy. Thus minimum of the dispersion relation (4.44) can only be found in $K_x = 0$ for arbitrary K_y.

4.3.8 Probability of recombination and luminescence spectra

We calculate the probability of recombination of the exciton in this section. We start with Fermi Golden Rule [15] which takes form of:

$$P_{i->f} \propto |\langle i|H_{int}|f\rangle|^2\delta(E - \hbar\omega), \qquad (4.84)$$

where $|i\rangle$ is an initial state and $|f\rangle$ is a final state. H_{int} is an interaction Hamiltonian and $\hbar\omega$ is the energy of emitted photon. In our case the initial state is an exciton in DQW and the final state is a state without electron in the conduction band and without hole in the valence band $|vac\rangle$. H_{int} has a standard form in the dipole approximation:

$$H_{int} \propto \mathbf{F}\mathbf{p}, \qquad (4.85)$$

where $\mathbf{p}$ is a momentum operator. Further manipulation can be made using envelope function framework and Slater determinants giving:

$$P_{i->f} \propto |\langle u_h|H_{int}|u_c\rangle|^2|\langle\chi_h|\chi_e\rangle|^2\delta_{\mathbf{K},\mathbf{0}}F(\mathbf{0})\delta(E_\nu - \hbar\omega), \qquad (4.86)$$

where u_h, u_e are the hole and electron periodic parts of the Bloch function at the zone centre of the host layer. χ_h, χ_e are tight-binding functions and $F(\mathbf{0})$, which is equal to:

$$F(\mathbf{0}) = \int_{-\infty}^{+\infty} \Psi(z_e = z, z_h = z, \mathbf{r}_\perp = \mathbf{0})dz, \tag{4.87}$$

is the overlap integral of the envelope functions of the electron and hole, $\Psi(z_e, z_h, \mathbf{r}_\perp)$ is the wave function of the exciton. We note that recombination is possible only for exciton with nearly zero momentum.

Since we are not interested in the absolute value of probability, but in the relative strength of the different transitions we will use this definition of the probability

$$P_i = \frac{F_i(\mathbf{0})}{\sum_j F_j(\mathbf{0})}, \tag{4.88}$$

where the summation runs over all transitions taken into account. We note that in the case of a wave function of this form:

$$\Psi = \sum_{ij} c_{ij}\Psi_{ij}, \tag{4.89}$$

where Ψ_{ij} are the wave functions of the direct and indirect exciton and c_{ij} are normalized, the probability of the recombination takes form of:

$$P_{|\Psi\rangle -> |vac\rangle} = \frac{1}{2}(c_{11}^2 + c_{22}^2). \tag{4.90}$$

We can now derive an expression for the intensity of luminescence knowing the relative probability of recombination. Our interest will be focused on phonon assisted transition to allow recombination of the k-space indirect excitons. We substitute $\delta_{\mathbf{K},\mathbf{0}}$ in eq. (4.86) by probability of the phonon-exciton interaction and we neglect the dependence of this probability on exciton momentum $\mathbf{K}$ [16]. Using this assumptions we can write luminescence intensity in arbitrary units:

$$I'(E) = \sum_i P_i\delta(E - E_i) \tag{4.91}$$

$$I(E) = \int_{-\infty}^{+\infty} I'(E')exp(-\beta E')G(E - E')dE', \tag{4.92}$$

where $G(E)$ is a function responsible for the peak widening, usually Gaussian or Lorentzian shape is used. $\beta = \frac{1}{k_B T}$, k_B is Boltzmann constant and T is temperature. This expression is valid if the main contribution to the widening of the spectral line comes from the fluctuation of the gap. If the main contribution originates from the dynamic disorder the luminescence intensity can be written as:

$$I(E) = exp(-\beta E) \int_{-\infty}^{+\infty} I'(E')G(E - E')dE' \tag{4.93}$$

The two expressions for $I(E)$ (eq. (4.91, 4.93) give nearly the same results for sufficiently large width of $G(E)$.

Chapter 5

Numerical and analytical treatment

In this chapter we show how we have treated the Hamiltonian (4.59), using the expansion (4.61) and derived equations (4.74), (4.79). We show also how to choose the phenomenological coefficients.

5.1 Analytical treatment

In this section we discuss solution of the Hamiltonian (4.59), whose theory is described in section (4.3.5). We discuss how to set phenomenological parameters. For a particle in the parabolic potential

$$V(r) = \frac{1}{2}m\omega^2 r^2, \tag{5.1}$$

we can write an equation for the mean radius for the lowest energy, which is

$$\langle r \rangle = \frac{1}{2}\sqrt{\frac{\pi\hbar}{m\omega}}. \tag{5.2}$$

Since for the phenomenological constants defined in eq. (4.49) we have $C_{(in)d} = \frac{1}{2}m\omega^2$ we rewrite eq. (5.2)

$$\langle r \rangle = \frac{1}{2}\sqrt{\frac{\pi\hbar}{2\sqrt{C_{(in)d}m}}}. \tag{5.3}$$

We adjust phenomenological parameters $C_{(in)d}$ to have the same radius in the analytical and numerical solution for both excitons (direct and indirect) without any fields. The parameters $S_{(in)d}$ are adjusted to have the same energy in both solutions. Since the radius of the direct exciton is smaller than for the indirect exciton, $C_d > C_{ind}$. The energy of the direct exciton is lower than that of the indirect exciton, which means $S_d > S_{ind}$.

The program for the solution of the Hamiltonian (4.59) is written in Fortran and for searching the eigenvalues and eigenvectors of the matrix the Jacobi subroutine is used

[17].

The accuracy of the solution could be better if we took into account higher levels of the harmonic oscillator. Using the fact that the solution can be found by the same procedure as in section (4.3.5), we can write the structure of the matrix for three lowest levels with quantum numbers $(n_x = 0, m_y = 0)$, $(1, 0)$, $(0, 1)$:

$$
\begin{pmatrix}
H_{00,00} & H_{00,10} & H_{00,01} \\
H^*_{00,10} & H_{10,10} & H_{10,01} \\
H^*_{00,01} & H^*_{10,01} & H_{01,01}
\end{pmatrix},
\tag{5.4}
$$

where the off-diagonal matrices have these properties

$$
H_{00,10(00,01)}(-B_\perp) = -H^*_{00,10(00,01)}(B_\perp); \qquad H_{10,01}(-B_\perp) = H^*_{10,01}(B_\perp)
\tag{5.5}
$$

and where

$$
H_{i,j} = \langle i | \hat{H} | j \rangle
\tag{5.6}
$$

and $\hat{H}$ is determined in (4.59).

5.2   Numerical treatment

5.2.1   Choice of the tight-binding functions

In this section we discuss the choice of the tight-binding functions $\varphi^j_{e(h)}(z_{e(h)})$ (4.25). We choose

$$
\varphi^j_{e(h)}(z_{e(h)}) = \sqrt{\frac{2}{d}} \cos \left[(z_{e(h)} - z^j_{e(h)}) \frac{\pi}{d} \right],
\tag{5.7}
$$

where z_j is the centre of the jth well and d is the width of the well (in this approximation we take zero width of the barrier). Other choices of the basis functions are also possible, we could use delta functions for example but as is shown in [4], this choice of basis functions is good only for narrow wells . On the contrary, our basis is well applicable even to wide wells.

In order to obtain tunnelling elements we can't simply use (4.28), that's why we adopt a different approach. We take the energy separation of the two first levels of the electrons (holes) in DQW for known barrier height and width. We get $\Delta_{e(h)} = 2t_{e(h)}$. The details and the dependence of $t_{e(h)}$ on d can be found in [2].

We also have to compute the potential matrix elements

$$
C_{ij} = \int dz_e dz_h \varphi_i^2(z_e) C(r_e - r_h) \varphi_j^2(z_h).
\tag{5.8}
$$

Integral of the Coulomb potential used in numerical treatment takes form of

$$
C_{22}(r) = \frac{4}{d^2} \int_0^d \int_0^d dz_e dz_h \frac{1}{4\pi\varepsilon \sqrt{(z_e - z_h)^2 + r^2}} \cos^2 \left[(z_e - \frac{d}{2}) \frac{\pi}{d} \right] \cos^2 \left[(z_h - \frac{d}{2}) \frac{\pi}{d} \right]
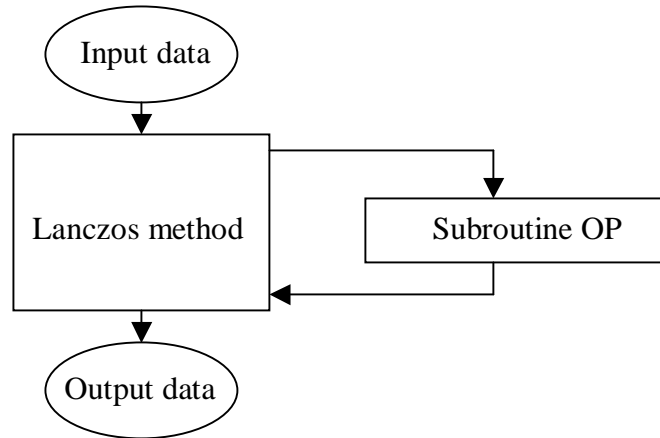\tag{5.9}
$$

Figure 5.1: Schematic draw of the program structure.

for C_{22}. If we introduce the following substitution

$$z_e - z_h = x$$
$$z_e + z_h = y \tag{5.10}$$

we can integrate over y and reduce the double integral to a simple integral. Other integrals C_{ij} can be treated analogically.

5.2.2 Structure of the program

In this section we describe the code of the program which numerically solves (4.74), (4.79). The program has two parts: the first part, written in C language, multiplies a matrix by a vector and the second part, written in Fortran, is the Lanczos method which computes eigenvalues and eigenvectors of large sparse symmetric matrices and calls the procedure written in C language.

The scheme of the program is shown in Fig. 5.1. The Lanczos method is called from the main program, the subroutine OP multiplies a matrix by a vector. Vector $\mathbf{u}_{Program}$ consists of 8 basic functions, real and imaginary part of u_{ij} (4.41):

$$\mathbf{u}_{Program} = \begin{pmatrix} \text{Re}(\mathbf{u}) \\ \text{Im}(\mathbf{u}) \end{pmatrix} \tag{5.11}$$

Since the Lanczos method is designed for real matrices, we use the following property of the Hermitian matrices:

$$\mathbf{A} = \mathbf{A}^*; \qquad \mathbf{B} \equiv \text{Re}(\mathbf{A}); \qquad \mathbf{C} \equiv \text{Im}(\mathbf{A}) \tag{5.12}$$

$$\mathbf{A}' = \begin{pmatrix} B & C \\ -C^T & B \end{pmatrix}, \tag{5.13}$$

where matrices $\mathbf{A}, \mathbf{A}'$ have the same eigenvalues and eigenvectors, but matrix $\mathbf{A}'$ has a twice degenerate spectrum of eigenvectors. We can see that if vector $(\mathbf{u}, \mathbf{v})$ is the eigenvector of the matrix $\mathbf{A}'$ belonging to the eigenvalue ε then also vector $(\mathbf{v}, -\mathbf{u})$ belongs to ε. We have slightly modified the code of the Lanczos method in order to eliminate computing twice the same.

Each vector component $\mathbf{u_{ij}^{R,I}}$ consists of the block of functions according to (4.61), where we cut the summation to $\sum_{k=-l}^{+l}$, thus there are $(2l+1)$ functions $f_k(r)$

$$\mathbf{u_{ij}^{R,I}} = \begin{pmatrix} f_{-l,ij}^{R,I}(r) \\ \vdots \\ f_{0,ij}^{R,I}(r) \\ \vdots \\ f_{+l,ij}^{R,I}(r) \end{pmatrix} \tag{5.14}$$

and each function $f_{k,ij}^{R,I}(r)$ is computed in a given range R with a given step dr, thus the program computes $N = [R/dr]$ points for each $f_{k,ij}^{R,I}(r)$. The total dimension of the vector (square matrix) is then (for the complex matrix):

$$\mathrm{Dim}(\mathbf{u}) = 8N(2l+1). \tag{5.15}$$

5.2.3 Boundary conditions and scalar product

We treat the boundary conditions in the following way. We start to compute at the point $dr/2$, which enables us to avoid the singularity of $\Delta_\perp$ in the origin of coordinates. For the second derivatives we use this boundary conditions:

$$f_{k,ij}^{R,I}(dr/2) = f_{k,ij}^{R,I}(dr/2) \ k \text{ even} \tag{5.16}$$
$$f_{k,ij}^{R,I}(dr/2) = -f_{k,ij}^{R,I}(dr/2) \ k \text{ odd} \tag{5.17}$$
$$f_{k,ij}^{R,I}((N+1)(dr - dr/2)) = 0, \tag{5.18}$$

which we have derived for $r \to 0$ and $r \to \infty$.

We have two different versions of the program which differ in the way how the scalar product of the vectors in the Lanczos method is treated. The scalar product takes form of:

$$\langle u(r)|v(r)\rangle = 2\pi \int_0^\infty u^*(r)v(r)rdr \tag{5.19}$$

in polar coordinates. We have chosen two ways how to cope with it. Our first approach is the transformation of the function $f_{k,ij}^{R,I}(r)$:

$$f_{k,ij}^{R,I}(r) = \frac{f_{k,ij}'^{R,I}(r)}{\sqrt{r}}. \tag{5.20}$$

New function $f_{k,ij}^{\prime R,I}(r)$ has a singularity in the first derivative in the origin (for small r and for the lowest energy this function has the same behaviour as the square root function). We also transform the operators in the Hamiltonian, namely $\Delta_\perp$ (for simplicity $f_{k,ij}^{\prime R,I}(r) \equiv \Phi'(r)$):

$$\Delta_\perp \Phi(r) = \left(\frac{1}{r} \frac{\partial}{\partial r} r \frac{\partial}{\partial r} - \frac{k^2}{r^2} \delta_{k,k_0} \right) \Phi(r) =$$

$$= \frac{1}{(dr)^2} \left[\frac{1 + \frac{dr}{2r}}{\sqrt{1 + \frac{dr}{r}}} \Phi'_+ - 2\Phi'_0 + \frac{1 - \frac{dr}{2r}}{\sqrt{1 - \frac{dr}{r}}} \Phi'_- \right] - \frac{k^2}{r^2} \delta_{k,k_0} \Phi'_0. \tag{5.21}$$

This operator is symmetric and treats well the singularity in the origin. $\Phi'_+, \Phi'_0, \Phi'_-$ are the function values in the points $(jdr + dr/2,\ jdr - dr/2,\ jdr - 3dr/2;\ j = 1..[R/dr])$. Our second approach consists in the change of the scalar product in the Lanczos method. Thus instead of:

$$\langle V|U \rangle = \sum_i V[i] * U[i] \tag{5.22}$$

we modify the code of the Lanczos method in the following way:

$$\langle V|U \rangle = \sum_i V[i] * U[i] * (i * dr - dr/2). \tag{5.23}$$

We also perform the reverse transformation of the wave function

$$\Phi' = \Phi \sqrt{r} \tag{5.24}$$

so that the operator $\Delta_\perp$ takes standard form of

$$\Delta_\perp \Phi'(r) = \frac{1}{(dr)^2} (\Phi_+ - 2\Phi_0 + \Phi_-) + \frac{1}{2rdr} (\Phi_+ - \Phi_-) - \frac{k^2}{r^2} \delta_{k,k_0} \Phi_0. \tag{5.25}$$

We have modified the Lanczos method to compute the eigenvalues and eigenvectors of special asymmetric matrices by changing the scalar product. We use the second approach in our program and the results of both approaches are almost the same. Generally we can say that the second approach gives slightly lower energies.

Chapter 6

Results

As was shown in section (4.3.7) the minimum of the energy is always found at $K_x = 0$ thus we do not discuss K_x in detail.

We use these parameters in our calculations:

$$
\begin{aligned}
m_e &= 0.0421 m_{e0} \\
m_h &= 0.34 m_{e0} \\
\varepsilon_r &= 12.5
\end{aligned}
$$

and we assume that the masses are the same in the well and in the barrier. Our choice of the parallel effective mass is discussed below.

6.1 Analytical results

In this section we use our analytical treatment described in sections (4.3.5) and (5.1) to qualitatively show what we may expect. We will show in the next section that the agreement can be very good between analytical and numerical results for some parameters and the energy of the ground state.

6.1.1 Phenomenological parameters

An appropriate estimation of the phenomenological parameters is required by the analytical model to work properly and give acceptable results. These parameters are obtained with the help of numerical results as energies and radii of exciton without any field and tunnelling.

Various parameters of the exciton in DQW are found in Table 6.1. These parameters are a function of the well width. We can notice that

$$\Delta E_{d,ind} = E_d - E_{ind} \tag{6.1}$$

practically doesn't depend on the width of the well (for the same M). In Table 6.2 calculated parameters are presented, where $E_{(in)d}^\omega$ is the energy of the harmonic oscillator.

Table 6.1: Radius and energy of the direct and indirect exciton as a function of the well width.

d[nm]	R_d[nm]	R_{ind}[nm]	E_d[meV]	E_{ind}[meV]	ΔE_{ind}[meV]
5.00	10.7	15.9	-10.0	-5.75	-4.26
7.50	11.5	18.3	-9.08	-4.70	-4.38
10.0	12.2	19.6	-8.37	-4.37	-4.37
12.5	12.8	21.0	-7.81	-3.49	-4.32

Table 6.2: $\omega_{(in)d}$, $E_{(in)d}^\omega$ and $S_{(in)d}$ as a function of the well width.

d[nm]	ω_d[10^{12}s^{-1}]	ω_{ind}[10^{12}s^{-1}]	E_d^ω[meV]	E_{ind}^ω[meV]	S_d[meV]	S_{ind}[meV]
5.00	21.8	9.9	14.3	6.5	24.3	12.3
7.50	18.9	7.7	12.4	5.1	21.5	9.8
10.0	16.8	6.5	11.0	4.3	19.4	8.3
12.5	15.3	5.7	10.0	3.7	17.8	7.2

6.1.2 Excitons in DQW without tunnelling

In this section we show the effect of the parallel magnetic field and electric field on DQW without tunnelling. Our calculations are done for a quantum well 7.5 nm wide and tunnelling elements $t_e = 3$ meV, $t_h = 0.05$ meV. These parameters are considered to be standard values. The parabolic dispersion relation of the direct and indirect exciton is shown in Fig. 6.1. In Fig. 6.2 the situation in the magnetic field $B_\parallel = 10$ T is shown. As indicated in eq. (4.44) the minimum of the dispersion relation of the indirect exciton is shifted from the origin by $\pm\frac{deB_\parallel}{\hbar} = 1.14$ nm^{-1}. In Fig. 6.3 the situation in the resonant electric field $F_{res} = (E_{ind} - E_d)/de = 5.6$ kV/cm is shown and we can see that the energy of the indirect exciton E_{12} has decreased by eF and is nearly on the same level as the energy of the direct exciton. The indirect exciton dispersion relation has its minimum lower than that of the direct exciton for an electric field stronger than F_{res}. The energies of the indirect exciton in an electric field stronger than F_{res} are always lower without magnetic field. The energy of the second indirect exciton increases by eF. In Fig. 6.4 the situation in the electric and magnetic field $F = 20$ kV/cm, $B_\parallel = 10$ T respectively is shown. We can see that one of the two
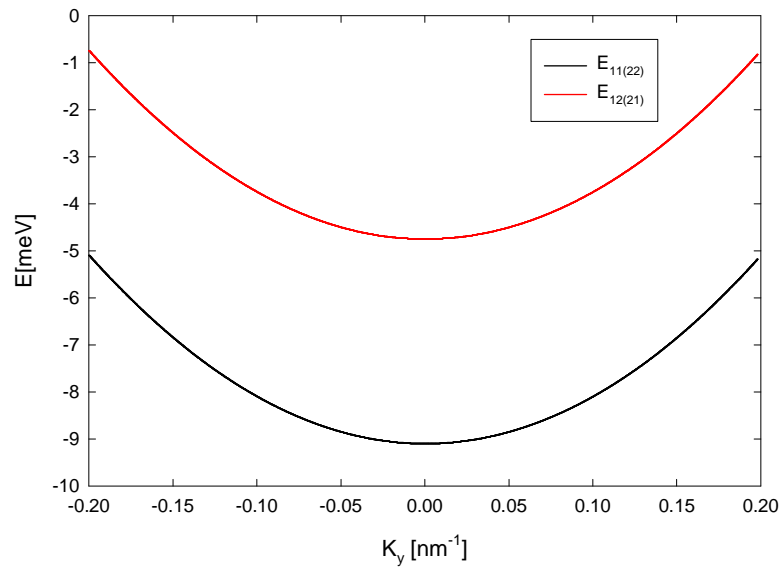
Figure 6.1: Dispersion relation of direct and indirect exciton in separated QWs. $E_{11(22)}$ ($E_{12(21)}$) is energy of direct (indirect) exciton.
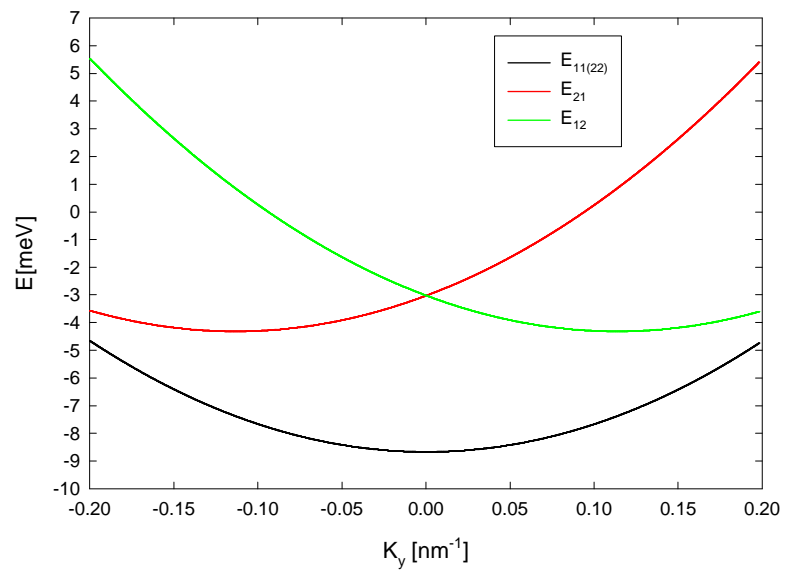

Figure 6.2: Dispersion relation of direct and indirect excitons in separated QWs in $B_{\parallel} = 10$ T.
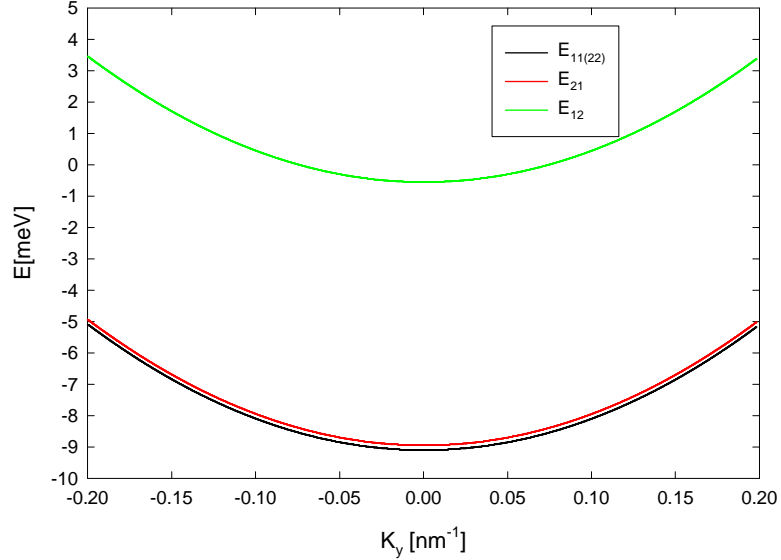
Figure 6.3: Dispersion relation of direct and indirect exciton in separated QWs in $F_{res} = (E_{ind} - E_d)/de = 5.6$ kV/cm.

indirect excitons has lower energy than direct excitons and the minimum of the energy is found in $-\frac{deB_\parallel}{\hbar} = -1.14$ nm^{-1}. We can conclude that if we want to have the energy minimum away off the origin, the electric and magnetic fields are both needed to be present.

6.1.3 DQW in weak magnetic field

If the magnetic and electric fields are switched on together we distinguish two interesting cases. In the first one we want to have maximal

$$E(\mathbf{0}) - E_{min}(\mathbf{K}) = \Delta E(\mathbf{K}) \tag{6.2}$$

for maximal $|\mathbf{K}|$ in order to reach possible Bose-Einstein condensation. We have two limits, a maximum magnetic field (12 T) accessible in the laboratory of the Institute of Physics and a maximum electric field which does not destroy the sample (about 20 kV/cm [2]). We take these tunnelling elements

$$
\begin{aligned}
t_e &= 3.0 \text{ meV} \\
t_h &= 0.05 \text{ meV}
\end{aligned}
$$

In Fig. 6.5 the dispersion relation is shown for parameters $F = 20$ kV/cm and $B_\parallel = 9$ T. It is evident that the curves differ only slightly in Fig. 6.5 and Fig. 6.4. We note
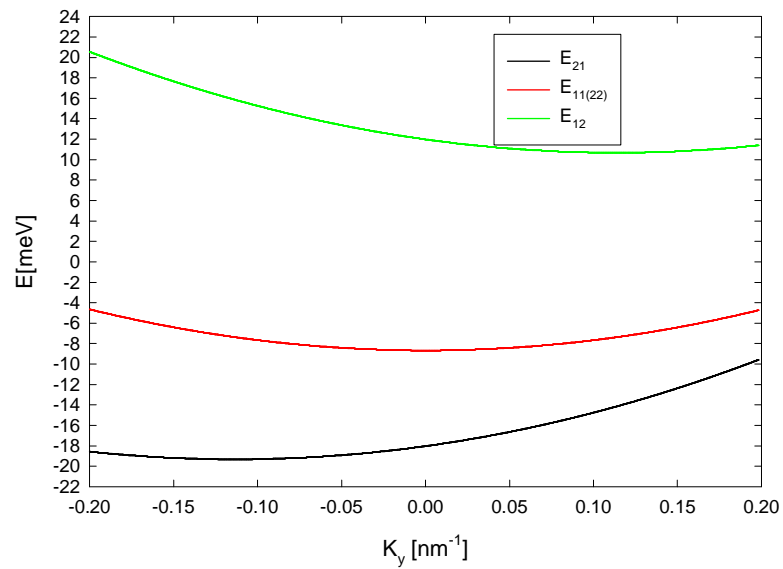
Figure 6.4: Dispersion relation of direct and indirect exciton in separated QWs in $F = 20$ kV/cm, $B_\parallel = 10$ T.
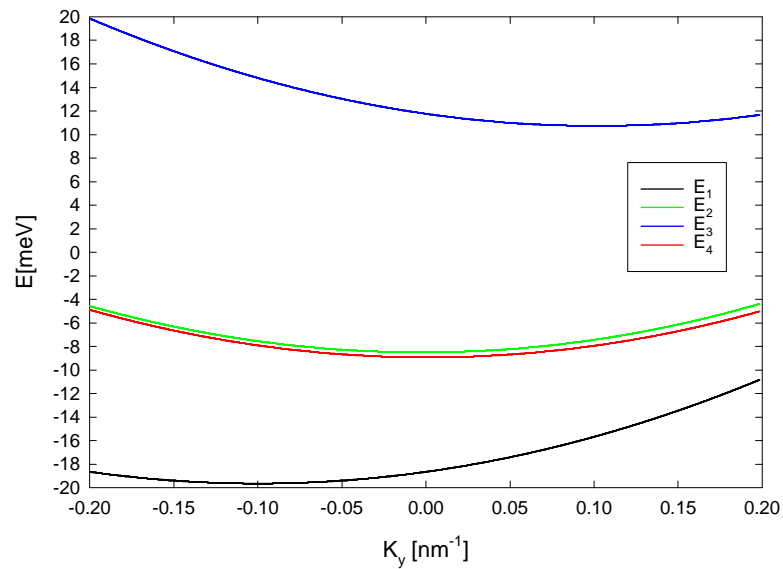

Figure 6.5: Dispersion relation of exciton in DQW in $F = 20$ kV/cm and $B_\parallel = 9$ T.

Table 6.3: Depth of the energy minimum and its position as a function of F for $B_\parallel = 9$ T and $B_\parallel = 12$ T.

F[kV/cm]	$\Delta E^9(\mathbf{K})$[meV]	$\Delta E^{12}(\mathbf{K})$[meV]	$K_y^{min,9}$[nm^{-1}]	$K_y^{min,12}$[nm^{-1}]
5.00	0.11	0.47	-0.038	-0.026
7.50	0.41	0.78	-0.074	-0.120
10.0	0.72	1.44	-0.090	-0.130
12.5	0.87	1.67	-0.096	-0.132
15.0	0.94	1.78	-0.098	-0.134
17.5	0.98	1.80	-0.100	-0.134
20.0	1.00	1.82	-0.100	-0.136
22.5	1.01	1.83	-0.102	-0.136

that the degeneracy of the direct exciton disappears due to tunnelling. The dependence of the $\Delta E(\mathbf{K})$ on electric and magnetic field is shown in Table 6.3. The results can be interpreted with the help of the figures from the previous section. The position of the minimum approaches the value $-\frac{deB_\parallel}{\hbar}$, which is -0.102 nm^{-1} for 9 T and -0.136 nm^{-1} for 12 T. The stronger the electric field the greater $\Delta E(\mathbf{K})$ is since we know that the energy of the indirect exciton decreases by eF. The maximum $\Delta E(\mathbf{K})$ is reached when the ground state is composed only of the indirect exciton and its value is $\hbar^2 \frac{K_y^2}{2M}$, which is 1.03 meV for 9 T and 1.91 meV for 12 T. The dependence of $\Delta E(\mathbf{K})$ on tunnelling

Table 6.4: Depth of the energy minimum and its position as a function of T_e for $B_\parallel = 9$ T, $F = 10$ kV/cm and $F = 20$ kV/cm.

T_e[meV]	$\Delta E^{10}(\mathbf{K})$[meV]	$\Delta E^{20}(\mathbf{K})$[meV]	$K_y^{min,10}$[nm^{-1}]	$K_y^{min,20}$[nm^{-1}]
0	1.04	1.04	-0.102	-0.102
1	0.98	1.04	-0.100	-0.102
2	0.84	1.02	-0.096	-0.102
3	0.72	1.00	-0.090	-0.100
4	0.62	0.97	-0.084	-0.098
5	0.55	0.93	-0.080	-0.098
6	0.50	0.89	-0.076	-0.096
7	0.47	0.85	-0.072	-0.094

is summarized in Table 6.4 and in Fig. 6.6 where the two lowest lying energy levels are depicted. The tunnelling mixes the direct and indirect exciton, and so even if the energy minimum shifts down with stronger tunnelling, the depth of the minimum is reduced.
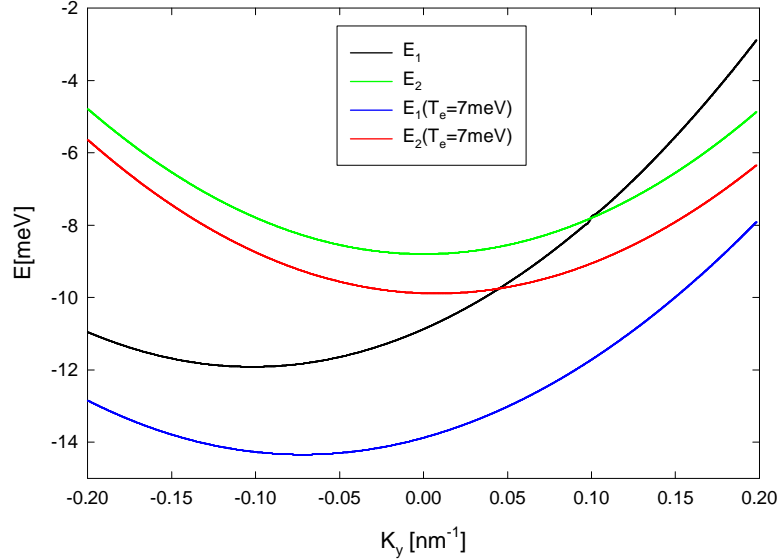
Figure 6.6: Dispersion relations of exciton in DQW in $F = 10$ kV/cm, $B_\parallel = 9$ T, $T_e = 0$ meV and $T_e = 7$ meV.

The dependence of $\Delta E(\mathbf{K})$ on the width of the well d is resumed in Tables 6.5 and 6.6. The depth increases with the well width since a wider well is equivalent to a stronger magnetic field. The validity of our model is limited by the condition

$$\Delta E_z^h = \Delta E_{xy},$$

where ΔE_z^h is the difference between the first two levels in z direction for heavy holes (assuming infinitely deep well) and ΔE_{xy} is the ground energy of the exciton. We get limiting width $d_{limit} = 20$ nm for our parameters. If we involved in our model higher states in z direction our model could be applicable to greater widths. In principle the width of the well and the whole structure is limited by the density of defects since we want to avoid large fluctuations of potential. Thus we get the width of the well $d_{limit} = 25$ nm for typical defect density 10^{15} cm^{-3}.

6.1.4 DQW in strong magnetic field

In this section we suppose we are not limited by the strength of magnetic field. What is interesting for us is shown in Fig. 6.7, where the second derivative of the energy with respect to K_y is equal to zero for $K_y = -0.12$ nm^{-1} and thus we may expect a singularity in the density of states. Such singularity exists in the electron density of states, which is discussed in detail in [1], [2] and [3]. Our objective is to find such parameters that the zero second derivative coincides with the minimum of the energy.

Table 6.5: Depth of the energy minimum and its position as a function of d for $B_\parallel = 12$ T, $F = 10$ kV/cm and $F = 20$ kV/cm, $T_e = 3$ meV.

d[nm]	ΔE^{10}[meV]	ΔE^{20}[meV]	$K_{y,10}^{min}$[nm^{-1}]	$K_{y,20}^{min}$[nm^{-1}]
5.00	0.25	0.68	-0.056	-0.084
7.50	1.44	1.82	-0.130	-0.136
10.0	3.20	3.30	-0.182	-0.182
12.5	5.16	5.17	-0.228	-0.228

Table 6.6: Depth of the energy minimum and its position as a function of d for $B_\parallel = 12$ T, $F = 10$ kV/cm and $F = 20$ kV/cm, $T_e = 6$ meV.

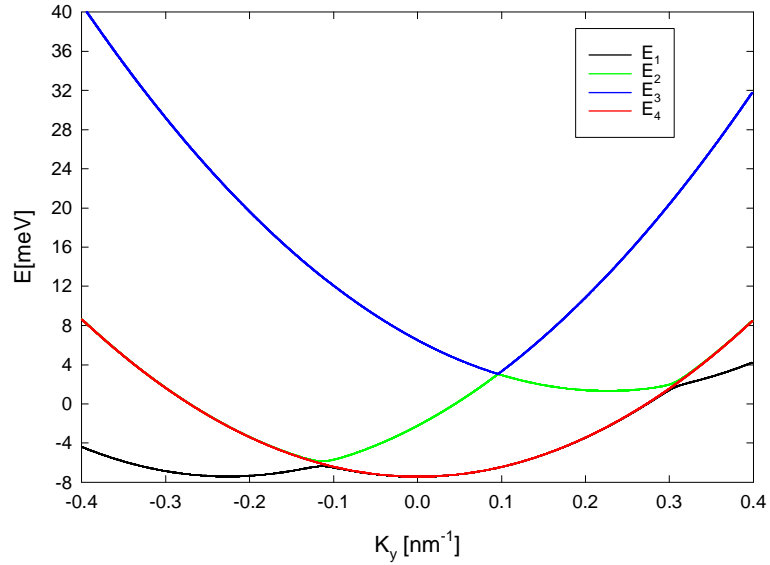| d[nm]	ΔE^{10}[meV]	ΔE^{20}[meV]	$K_{y,10}^{min}$[nm^{-1}]	$K_{y,20}^{min}$[nm^{-1}]	ΔE[meV]	K_y^{min}[nm^{-1}]
5.00	0.23	0.51	-0.050	-0.074	0.84	-0.91
7.50	1.05	1.71	-0.116	-0.136	1.91	-0.136
10.0	3.08	3.28	-0.180	-0.182	3.34	-0.181
12.5	5.15	5.18	-0.228	-0.228	5.21	-0.226

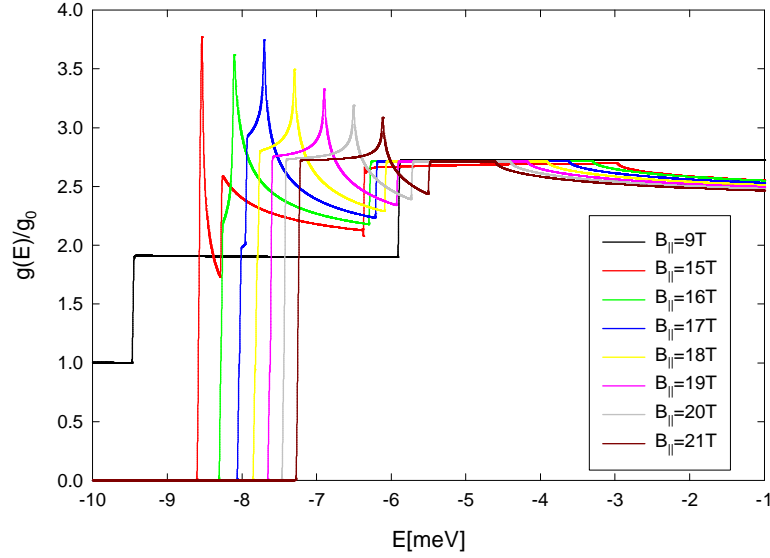Figure 6.7: Dispersion relations of exciton in DQW in $F = 5.8$ kV/cm, $B_\parallel = 20$ T.

Figure 6.8: Density of states of exciton in DQW in $F = 5.8$ kV/cm.

In Fig. 6.8 the density of states is shown for various $B_\parallel$. Two dimensional density of states is equal to:

$$g_0 = \frac{M}{\pi \hbar^2} = 1.56 \times 10^{-3} \text{meV}^{-1} \text{nm}^{-2}$$

for weak magnetic fields and has a step like behaviour. When the singularity in the density of states is found in the minimum of the energy the corresponding magnetic field is called critical $B_\parallel^C$. In our case the critical field is found in the interval $< 15\,T, 16\,T >$. We can observe the development of the singularity. Nothing interesting happens up to 10 T then the step like behaviour changes and the lowest step starts to decrease and has a local maximum and minimum and thus a sharp spike is formed. The second step develops a smoother spike. This behaviour continues to the moment when the first step disappears and the singularity coincidences with the minimum of the second step (which has become the first step). This situation is shown for 15 T. In Fig. 6.9 the dispersion relation is plotted for different strength of tunnelling. We can see that critical magnetic field increases with stronger tunnelling.

6.1.5   DQW in $B_\perp$

In this section we discuss the influence of $B_\perp$ on the dispersion relation. Since we use only an approximate model, whose limits exhibit for $B_\perp \neq 0$, the conclusions of this section are only qualitative. In Table 6.7 the dependence of the total mass of the exciton on $B_\perp$ is shown. If $B_\parallel = 0$ T and $F = 0$ kV/cm then the minimum of the dispersion
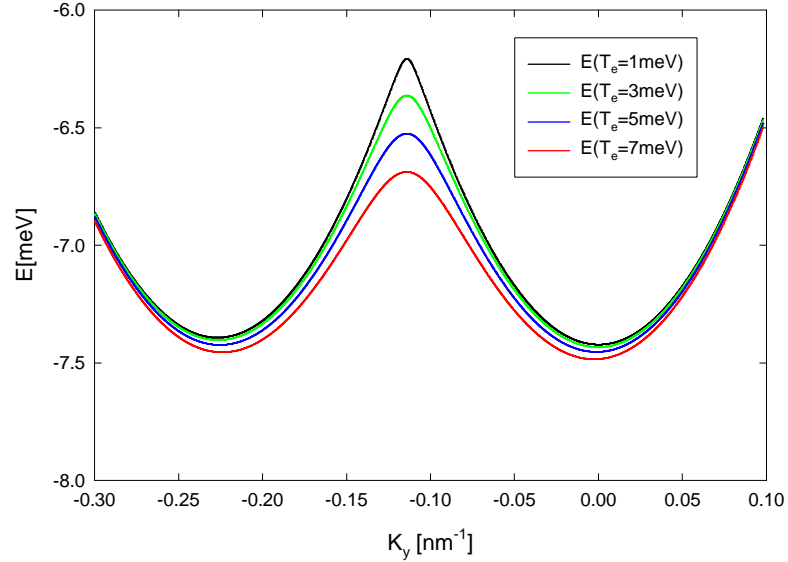
Figure 6.9: Dispersion relations of exciton in DQW in $F = 5.8$ kV/cm, $B_\parallel = 20$ T for different strength of tunnelling.

relation is found at $\mathbf{K} = \mathbf{0}$ and $B_\perp$ only changes the curvature of the parabola. In

Table 6.7: Dependence of the total mass of the exciton on $B_\perp$.

.

$B_\perp$[T]	0	4	8	12	16	20
M[m_{e0}]	0.3821	0.3836	0.3889	0.3939	0.3975	0.4000

Fig. 6.10 the dispersion relation as a function of $B_\perp$ is shown. The parabola of the indirect exciton increases faster with $B_\perp$ (due to lesser binding) than the parabola of the direct exciton and we see that side minimum gradually disappears.

6.1.6   Different effective masses

In this section we show the dependence of $\Delta E(\mathbf{K})$ on electron effective mass. Parameters of direct and indirect exciton a function of effective mass are listed in Table 6.8. The binding energy increases with the mass of the electron and thus the radius shrinks. Depth of the energy minimum, B^C and F_{res} as a function of m_e are shown in Table 6.9. As we may expect the position of the minimum is not affected by the effective mass. The depth of the minimum is proportional to $1/M$ and thus decreases with the mass. Since $F_{res} = (E_d - E_{ind})/de$, F_{res} increases with the mass.
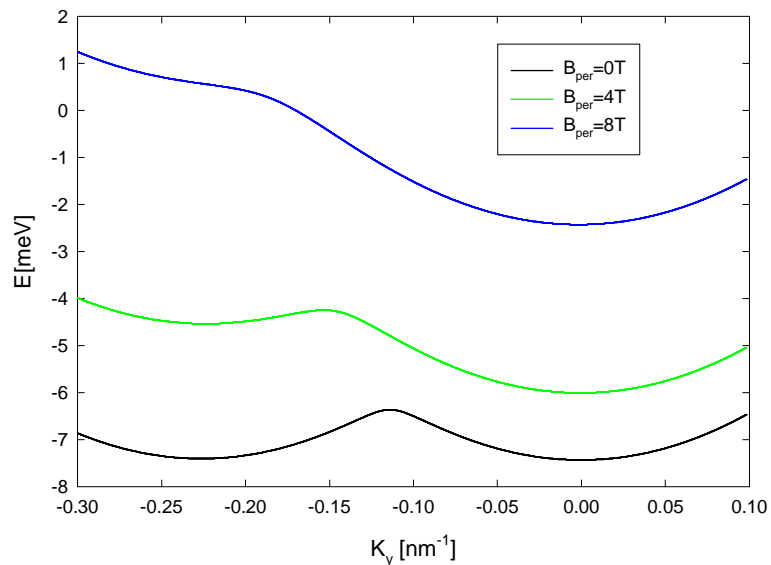
Figure 6.10: Dispersion relation of exciton in DQW in $F = 5.8$ kV/cm, $B_\parallel = 20$ T as a function of $B_\perp$.

Table 6.8: Radius and energy of the direct and indirect exciton as a function of the electron effective mass.

$m_e[\mathrm{m}_{e0}]$	$R_d[\mathrm{nm}]$	$R_{ind}[\mathrm{nm}]$	$E_d[\mathrm{meV}]$	$E_{ind}[\mathrm{meV}]$	$\Delta E_{ind}[\mathrm{meV}]$
0.0421	11.5	18.3	-9.08	-4.70	-4.38
0.0670	8.3	14.8	-12.18	-5.69	-6.49
0.1000	6.5	12.5	-15.20	-6.48	-8.72

Table 6.9: Depth of the energy minimum, its position, an interval of critical magnetic fields B^C and F_{res} as a function of m_e.

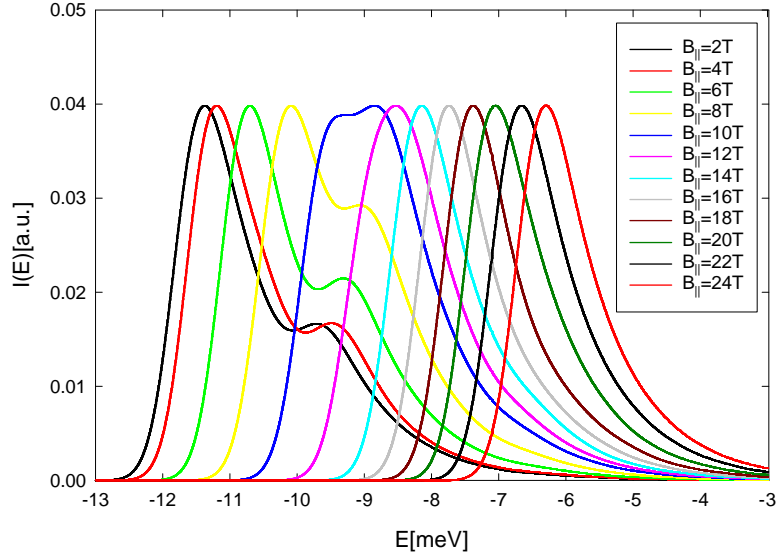| $m_e[\mathrm{m}_{e0}]$	$\Delta E^{20}[\mathrm{meV}]$	$K_{y,20}^{min}[\mathrm{nm}^{-1}]$	$B^C[\mathrm{T}]$	$F_{res}[\mathrm{kV/cm}]$
0.0421	1.82	-0.136	$\langle 15.0;16.0 \rangle$	5.8
0.0670	1.59	-0.132	$\langle 17.0;18.0 \rangle$	8.6
0.1000	1.32	-0.128	$\langle 18.5;19.5 \rangle$	11.5

Figure 6.11: Intensity of luminescence as a function of energy and magnetic field, $\Gamma = 0.4$ meV.

6.1.7 Luminescence spectra

In this section we show luminescence spectra calculated using eq. (4.91). We calculate only the contribution of the exciton recombination to the luminescence spectra, the gap of GaAs and energy shift caused by energy quantization of electrons and heavy holes in z direction should be added to obtain measurable values (only first subbands should be taken into account). The luminescence spectra are shown in Fig. 6.11. These spectra are calculated for $T = 10$ K and the width of the Gaussian function is $\Gamma = 0.4$ meV. In Fig. 6.12 the luminescence spectra with the width $\Gamma = 1.5$ meV are shown. Electric field is in resonance $F = F_{res} = 5.8$ kV/cm. The spectra are renormalized to the maximum intensity. We can see two peaks for weak magnetic field which join together in magnetic field B=12 T. In resonance (around 16 T) there is only one peak which moves with the diamagnetic shift. If we measured the spectra we could multiply each spectra by Boltzmann factor and we would get as a result the convolution of the density of states, probability of recombination and Gaussian function. This is shown (derived from Fig. 6.11) in Fig. 6.13 where the singularity can be seen clearly for $B_{\parallel} = 18$ T. Finally Fig. 6.14 shows the probabilities of recombination for four levels of analytical model as a function of the parallel magnetic field. The probabilities are calculated using eq. (4.88) and eq. (4.90). The behaviour of the probabilities is as expected since the parabola of the indirect exciton is shifted from the origin with parallel magnetic field and thus the first two energies with $\mathbf{K} = \mathbf{0}$ are mainly composed of direct exciton.
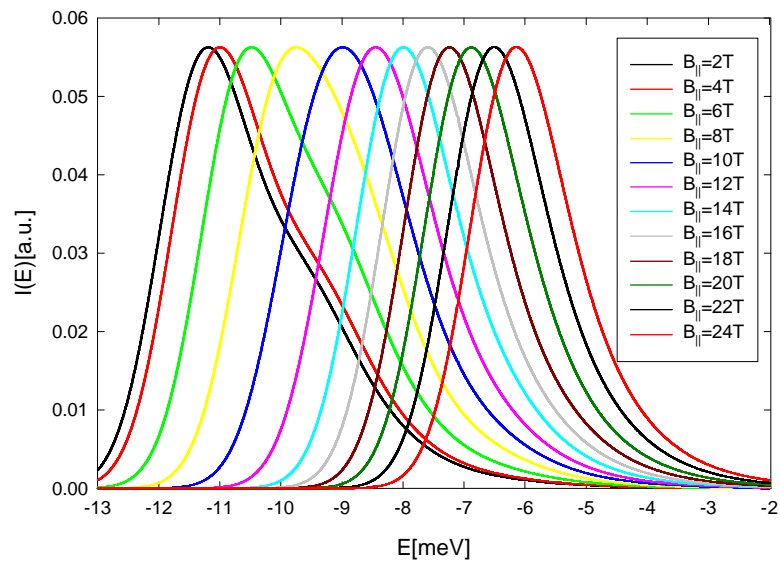
Figure 6.12: Intensity of luminescence as a function of energy and magnetic field, $\Gamma = 1.5$ meV.
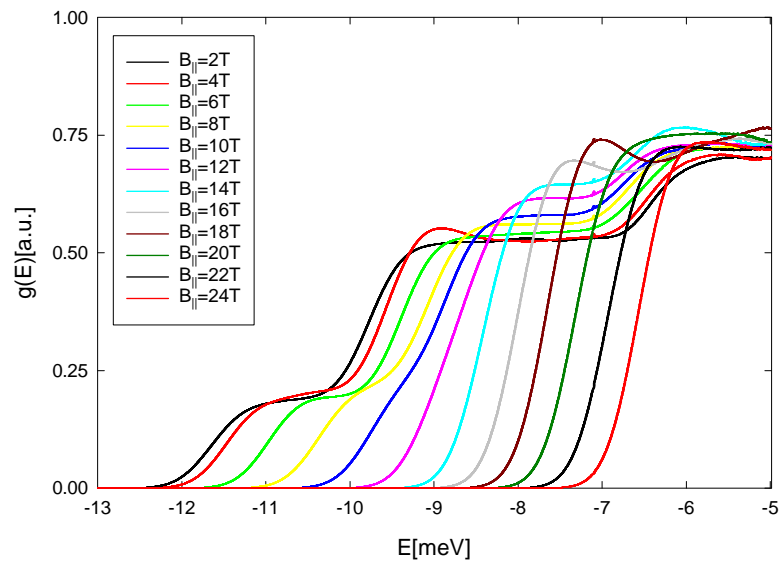

Figure 6.13: Convolution of the density of states with Gaussian function.
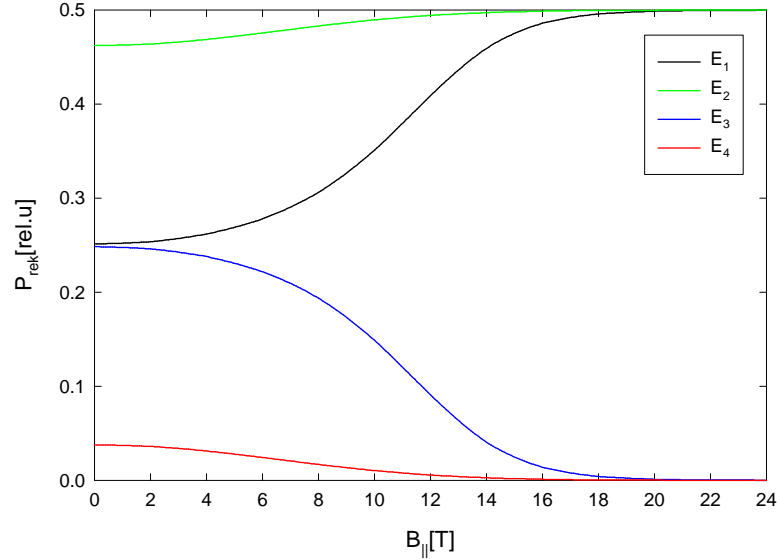
Figure 6.14: Probability of recombination as a function of magnetic field.

6.2 Numerical results

In this section we discuss the numerical solution. We use these standard parameters (tunnelling elements for electrons and holes, range of computation for r, step of r, number of angular momentum eigenfunctions):

$$
\begin{aligned}
t_e &= 3.0\text{meV} \\
t_h &= 0.05\text{meV} \\
R &= 70\text{nm} \\
dr &= 1\text{nm} \\
l &= 4.
\end{aligned}
$$

6.2.1 Correspondence between numerical and analytical results

In this section we show limits of analytical calculations. The dispersion relation calculated numerically and analytically is shown in Fig. 6.15. As we can see only energies of the lowest lying level agree as well as we expected. The agreement is at its best if $B_\perp = 0$ T since the deviation in energies is induced only by tunnelling elements, which is significant only in very strong magnetic field. Other disadvantage of the analytical treatment is caused by the fact that for strong electric field the excited exciton levels appear. This is significant mainly for the indirect exciton as we will see below since the
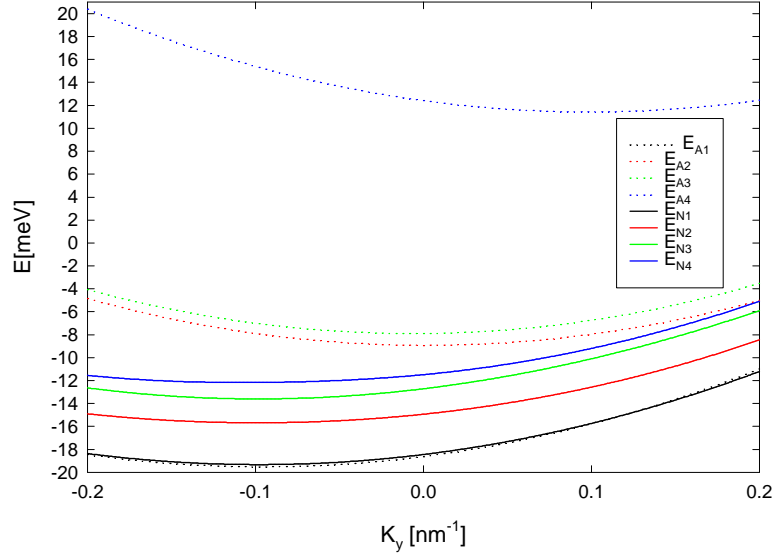
Figure 6.15: Dispersion relation of exciton in DQW in $F = 20$ kV/cm, $B_\parallel = 8.9$ T and $B_\perp = 1.5$ T calculated numerically (solid line) and analytically (dashed line).

second energy level of the indirect exciton has an approximate value of $E_1/9$ (supposing a behaviour similar to the two dimensional hydrogen atom).

In Fig. 6.16 a comparison of two dispersion relations is shown. The agreement is relatively good for weak $B_\perp$ but analytical results gradually start to be unreliable and they preserve only qualitatively the properties of numerical solution, as is the growth of the total mass of the exciton with $B_\perp$. This increase is underestimated in analytical calculations. The disagreement has its physical reason since the mean electron-hole distance increases with their momentum. This means that they feel a stronger potential, but the growth of the parabolic potential is much faster than that of the Coulomb one. In Fig. 6.17 the dispersion relation in strong perpendicular magnetic field is shown and effective masses of the first and third energy level are

$M^1_{eff} = 0.48 m_{e0}$
$M^3_{eff} = 0.81 m_{e0}$.

Detailed comparison of three dispersion relations is shown in Fig. 6.18. We can conclude that analytical and numerical results are in a very good agreement (difference is less than 5%) and this enables us to accept analytical results as valid and beneficial. Therefore we can avoid numerical computing in the vicinity of the singularity where the Lanczos method calculates very slowly.
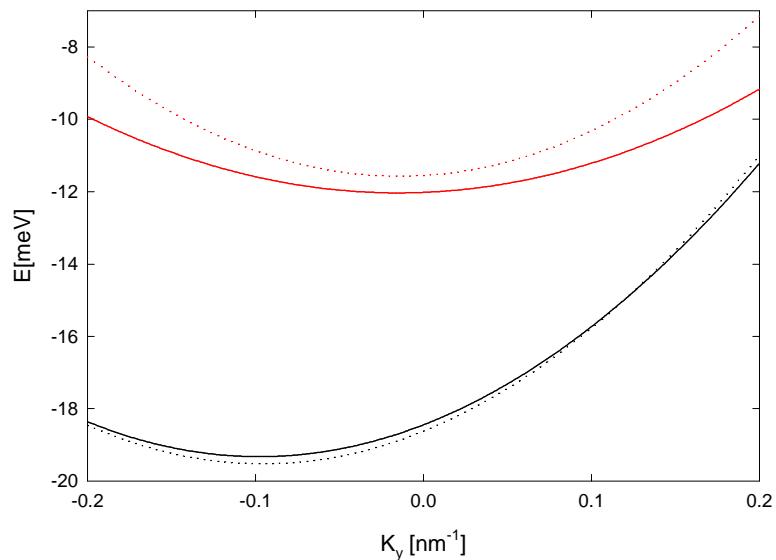
Figure 6.16: Dispersion relation of exciton in DQW in $F = 20$ kV/cm, $B_{\parallel} = 8.9$ (1.5) T and $B_{\perp} = 1.5$ (8.9) T in black (red) calculated numerically (solid line) and analytically (dashed line).
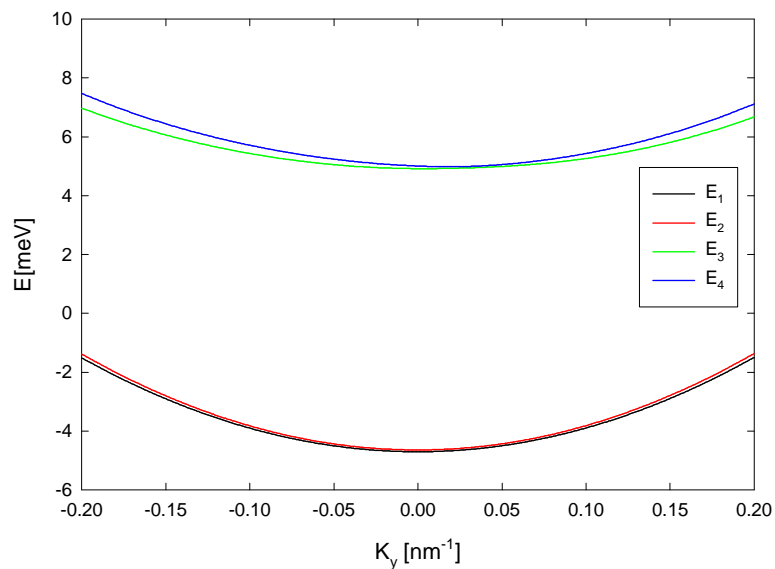

Figure 6.17: Dispersion relation of exciton in DQW in $B_{\parallel} = 1.5$ T and $B_{\perp} = 8.9$ T calculated numerically.
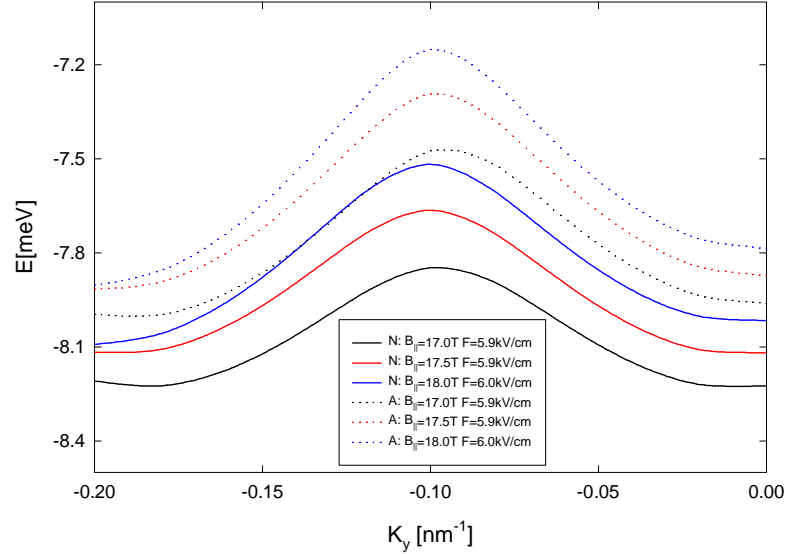
Figure 6.18: Dispersion relation of exciton in DQW calculated numerically (solid line) and analytically (dashed line) for various fields.

6.2.2   Charge density

In this section we show charge densities of the exciton. They are plotted in Fig. 6.19. First we discuss charge densities calculated for parameters $B_\perp = 0$ T, $B_\parallel = 17.5$ T, $F = 5.9$ kV/cm, $K_x = 0$ nm^{-1}, a) $K_y = -0.02$ nm^{-1} and b) $K_y = -0.18$ nm^{-1}. Since we are close to the singularity in the density of states, charge density smoothly proceeds from being predominantly composed of indirect exciton (b) to be composed of direct exciton (a) and the energy does not almost change. The charge density of the indirect exciton is less localized than that of the direct exciton.

Now we discuss charge densities calculated for parameters $B_\perp = 8.9$ T, $B_\parallel = 1.5$ T, $F = 20$ kV/cm, $K_x = 0$ nm^{-1}, c) $K_y = 0.18$ nm^{-1} and d) $K_y = -0.18$ nm^{-1}. As we can see the charge density of (d) is the same as the charge density of (c) if we exchange x, y for $-x, -y$, which is equivalent to exchanging $B_\parallel$ for $-B_\parallel$ or K_y for $-K_y$. In other words we may say that magnetic field turns opposite charges in opposite directions perpendicular to their velocity. We can also note that $B_\perp \neq 0$ deforms the angular symmetry of the charge density.

Last we discuss charge densities calculated for parameters $B_\perp = 1.5$ T; $B_\parallel = 8.9$ T; $F = 20$ kV/cm; $K_x = 0$ nm^{-1}, $K_y = 0.2$ nm^{-1}. These densities are calculated for different gauge of the magnetic field and thus should not differ. As we can see they are almost identical.
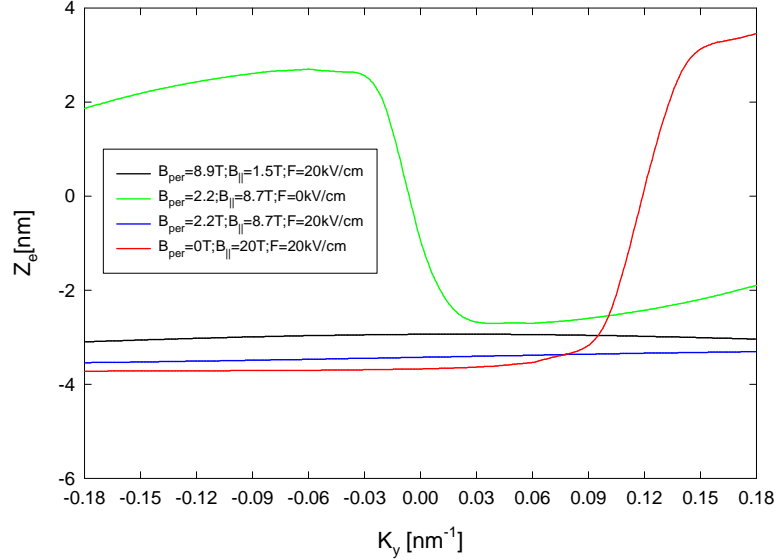
Figure 6.20: Z coordinate of the electron as a function of K_y for various parameters.

6.2.3 Properties of exciton in DQW

In this section we show the dependence of the mean value of Z_e, Z_h and of the radius of exciton R_{exc} on K_y for various parameters and for the ground state. Z coordinate of the electron is shown in Fig. 6.20, z coordinate of the hole in Fig. 6.21 and the radius of the exciton in Fig. 6.22. As we can see, the black line ($B_\perp = 8.9$ T, $B_\parallel = 1.5$ T, $F = 20$ kV/cm) depends on K_y the less since the ground state is bound only weakly with other states and is mainly composed of the indirect exciton whose parameter dependence on K_y is weak in strong $B_\perp$ as is discussed in chapter 7. Electron and hole are in different wells due to applied electric field. The radius is small for indirect exciton as $B_\perp$ shrinks the exciton and its dependence on K_y is small.

Z_e corresponding to the green line ($B_\perp = 2.2$ T, $B_\parallel = 8.7$ T, $F = 0$ kV/cm) is nearly symmetrical with respect to the origin. The asymmetry is caused mainly by numerical precision. Energies are symmetric with a deviation lower than 1% and all mean values are also symmetric with a deviation lower than 5% for $|K_y| > 0.02$ nm^{-1}. The reason of the asymmetry in the vicinity of $|K_y| = 0$ nm^{-1} is a rapid change of the wave function from one well to the another one since the exciton in the left well with momentum K_y must have the same energy as the exciton in the right well with momentum $-K_y$.

Z_e corresponding to the blue line ($B_\perp = 2.2$ T, $B_\parallel = 8.7$ T, $F = 20$ kV/cm) is in the left well and Z_h in the right well due to the applied electric field, thus the ground state is composed mainly of the indirect exciton. Z_e increases as direct exciton is more involved in the ground state. The radius of the exciton is smaller than for indirect exciton without field because $B_\perp$ shrinks the exciton. The radius does not decrease
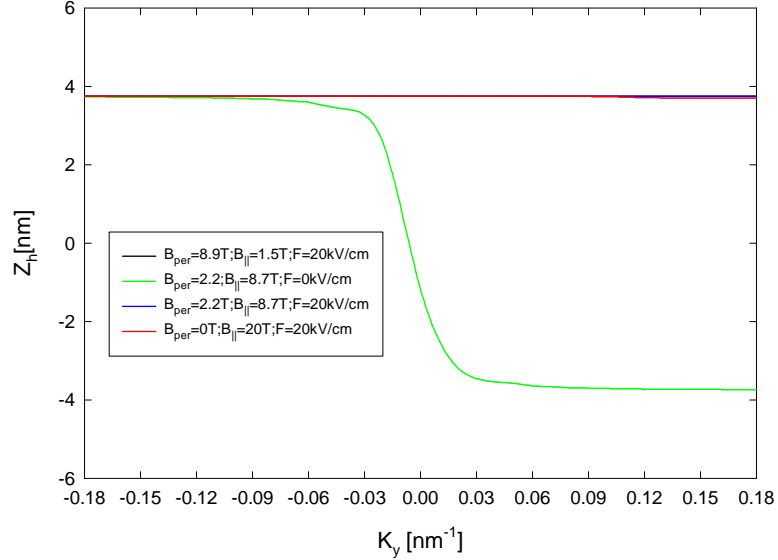
Figure 6.21: Z coordinate of the hole as a function of K_y for various parameters.

as we could expect due to increasing mixing with direct exciton but increases since indirect exciton is less localized than direct exciton and it delocalizes faster with K_y in $B_\perp$, which is not compensated by tunnelling.

Z_e corresponding to the red line ($B_\perp = 0$ T, $B_\parallel = 20$ T, $F = 20$ kV/cm) changes the well (Z_h does not change the well) when the parabolas of the indirect and direct exciton intersect. We can observe the same behaviour for the radius which sharply decreases.

6.2.4 Probability of recombination of exciton

In this section we show the dependence of the probability of exciton recombination as a function of various parameters for the first four levels. The probabilities are calculated using eq. (4.88). In Fig. 6.23 the probabilities and in Fig. 6.24 the energies of the recombination as functions of electric field are shown. We can see that the probability of exciton recombination of the first level decreases with the magnitude of the field since indirect exciton is more involved in this level. The probability of recombination of the third level increases, since the mixing of direct and indirect exciton is stronger, to the point when this level is predominantly composed of excited indirect exciton level. The fourth level is composed of the second ground indirect exciton level for a weak electric field ($F_z < 2$ kV/cm), excited indirect exciton levels appear for stronger fields. When $F_z = 8$ kV/cm the third and fourth level are formed only by excited indirect exciton levels. These levels crossover the direct exciton level in $F_z = 12$ kV/cm.
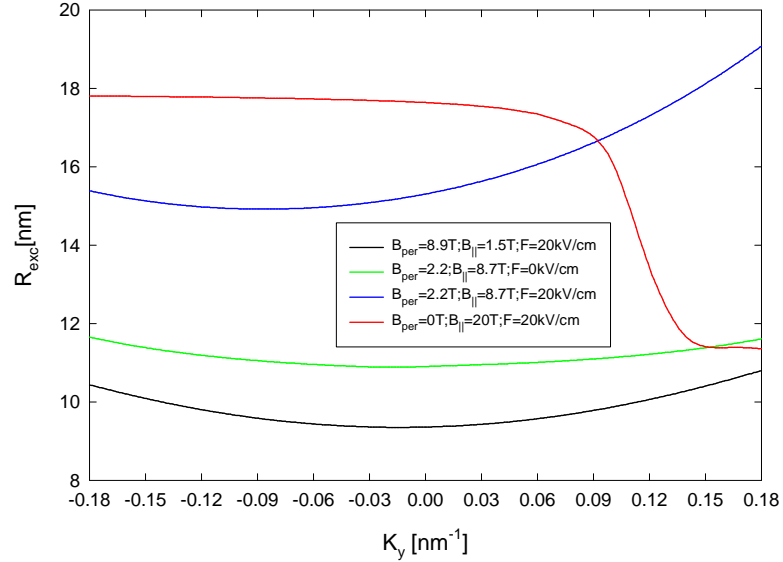
Figure 6.22: Radius of the exciton as a function of K_y for various parameters.

Only the fourth level is composed of direct exciton to the point when the intersection between this level and the indirect exciton level with nearly zero binding energy occurs in $F_z = 14$ kV/cm. Since we calculate only relative probabilities, we loose information when the direct exciton level disappears.

In Fig. 6.25 the probabilities and in Fig. 6.26 the energies of the recombination as functions of magnetic field are shown (magnetic field is constant, we only change its direction) for $F = 20$ kV/cm. The first (second) level is mainly composed of the ground (excited) indirect exciton level. The third level is composed of the second excited indirect exciton level, whose energy increases very rapidly with $B_\perp$, for $B_\perp < 1.5$ T. The fourth level is composed of excited indirect exciton level with nearly zero binding energy to the point where it intersects with the third level (1.5 T) then the role of the third and fourth level is exchanged. In $B_\perp = 2.5$ T there is a crossover of the second excited indirect exciton level (fourth level) with the ground direct exciton level. The information about the probabilities is recovered as shows the sharp increase of the fourth level probability. In $B_\perp = 5.5$ T the fourth level intersects with the third one and the ground direct exciton level becomes the third level. The second ground direct exciton level is continuously involved in the fourth level. These crossovers can be observed in the probability peaks and dips.

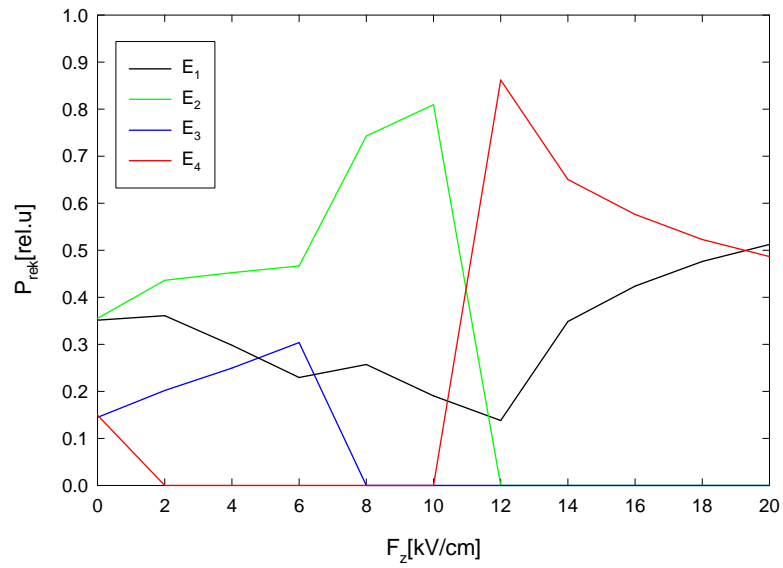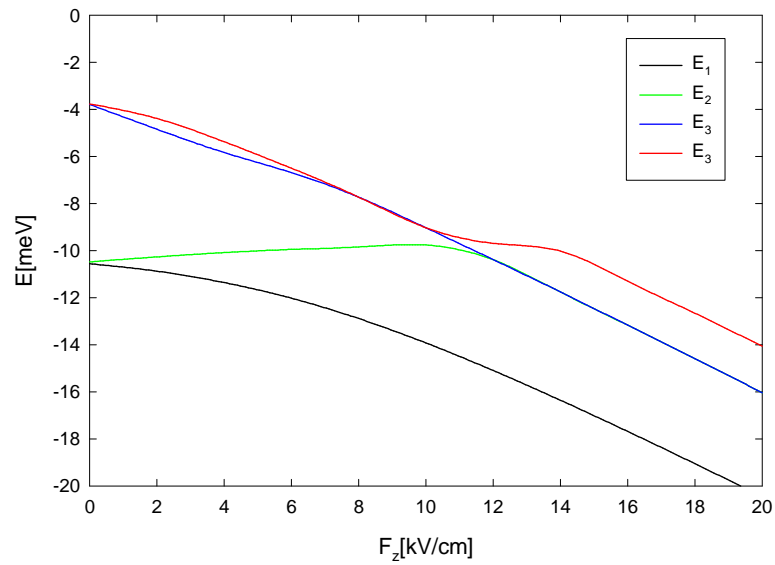Figure 6.23: Probability of recombination as a function of F_z for the first four levels.

Figure 6.24: Energy of the first four levels as a function of F_z.
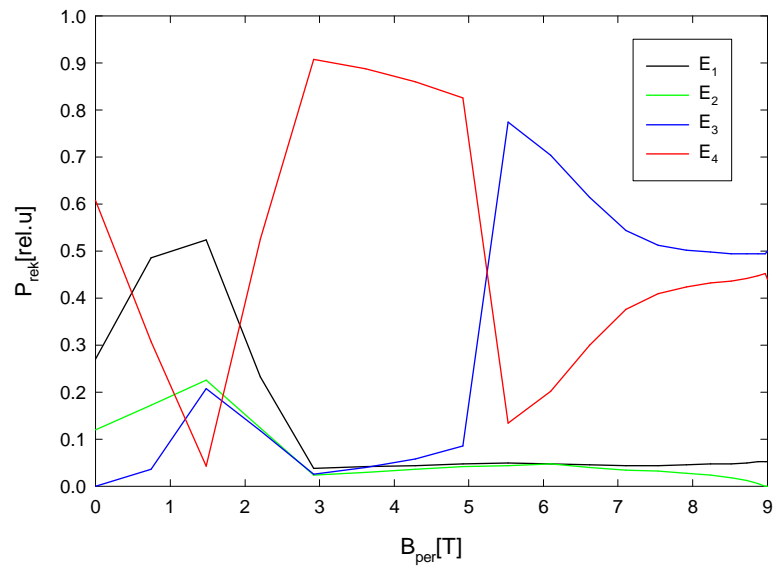
Figure 6.25: Probability of recombination as a function of $B_\perp$ ($|\mathbf{B}| = 9$ T being constant) for the first four levels.
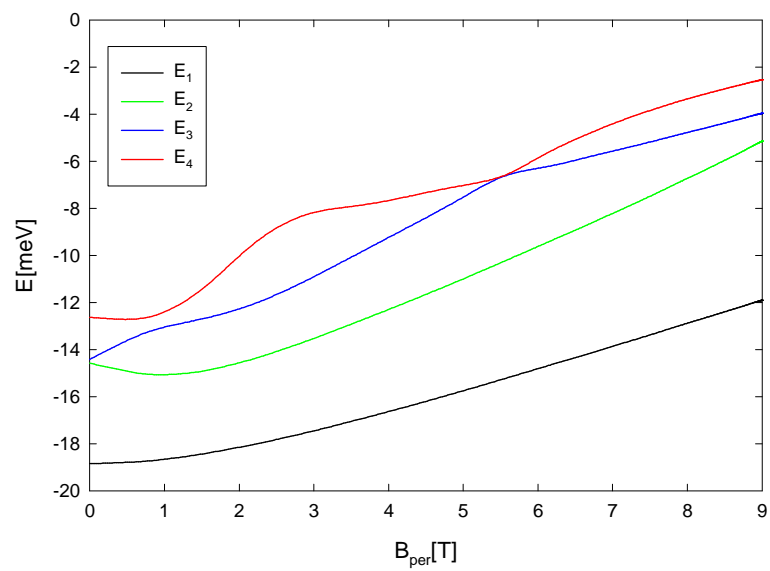

Figure 6.26: Energy of the first four levels as a function of $B_\perp$ ($|\mathbf{B}| = 9$ T being constant).
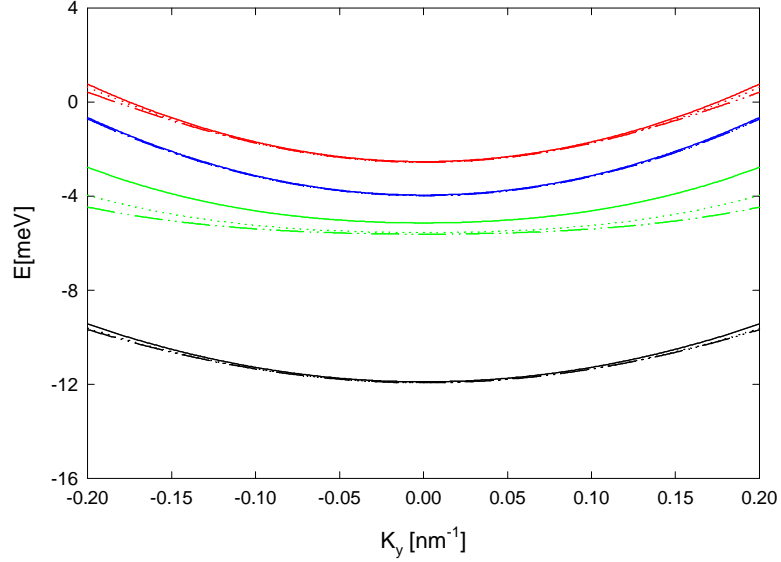
Figure 6.27: Dispersion relation calculated for different l and for $B_\perp = 9$ T, $B_\parallel = 0$ T, $F = 20$ kV/cm, $l = 4$ solid line, $l = 6$ dotted line, $l = 8$ dash-dotted line.

6.2.5 Numerical precision

In this section we show the influence of the parameter choice on the precision of the results. The dispersion relations, which are shown in Fig. 6.27, are calculated for the same parameters $B_\perp = 9$ T, $B_\parallel = 0$ T, $F = 20$ kV/cm only l (number of considered angular momentum eigenfunctions) is varied, which changes the results. As we can see only the second level differs visibly. Since we are dominantly interested in $B_\parallel$ we can conclude that $l = 4$ is sufficient. Larger l is convenient in the case of strong $B_\perp$, in such case $l = 6$ should be sufficient. The dispersion relations, which are shown in Fig. 6.28, are calculated for the same parameters $B_\perp = 1.5$ T, $B_\parallel = 8.9$ T, $F = 20$ kV/cm but for different gauges of the magnetic field. Symmetric (solid line) and asymmetric (dotted line) gauges give nearly the same results. Calculated energies are shown in Table 6.10 for parameters: A ($B_\perp = 10$ T, $B_\parallel = 7$ T, $F = 0$ kV/cm, $K_x = 0$ nm^{-1}, $K_y = 0$ nm^{-1}), B ($B_\perp = 10$ T, $B_\parallel = 7$ T, $F = 0$ kV/cm, $K_x = 0.6$ nm^{-1}, $K_y = 0.6$ nm^{-1}). We can note that for larger K_x, K_y the agreement is not so good but this difference occurs in the region where we usually do not calculate. We can consider this limited agreement as a confirmation of the acceptable reliability of numerical results.

Table 6.10: Energy levels calculated for asymmetric and symmetric gauge of the magnetic field, for parameters A, B see text on page 59.

	A_s	A_n	B_s	B_n
$E_1[\text{meV}]$	-3.59	-3.51	35.3	35.1
$E_2[\text{meV}]$	-3.53	-3.45	40.4	41.2
$E_3[\text{meV}]$	5.80	5.89	42.0	42.3
$E_4[\text{meV}]$	6.47	6.42	48.3	46.9

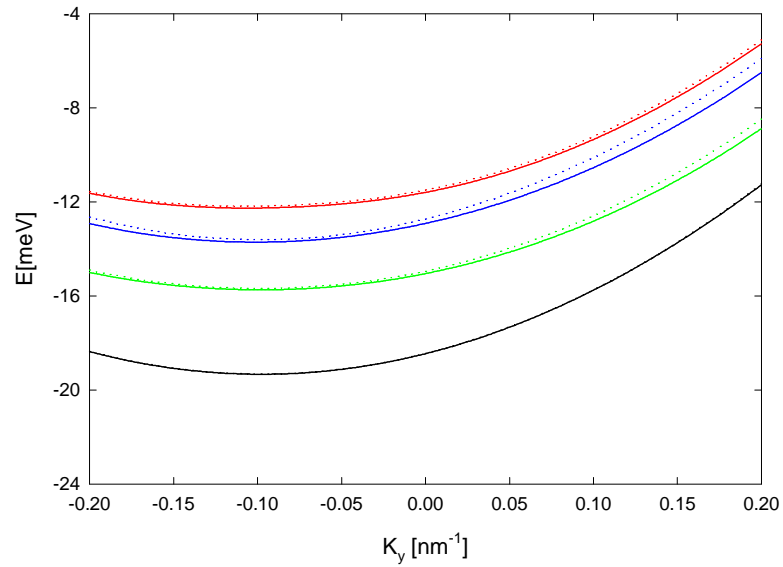
Figure 6.28: Dispersion relation calculated for different gauge of the magnetic field and for $B_\perp = 1.5$ T, $B_\parallel = 8.9$ T, $F = 20$ kV/cm, asymmetric gauge (solid line) and symmetric gauge (dotted line).

Chapter 7

Discussion

First we interpret the asymmetry in the dispersion relation of the exciton in the magnetic and electric field. Exciton which is indirect in the r-space induces an electric dipole ed. This induced electric dipole when moving induces a magnetic dipole $edv = ed\hbar K/M$ perpendicular to the velocity, which interacts with the parallel magnetic field. This interaction contributes to the Hamiltonian by a term linear in $\mathbf{K}$ $(\hat{h}_{12}(\hat{\mathbf{k}}, \mathbf{K} - e_y \frac{deB_\parallel}{\hbar}, \mathbf{r})$, eq. (4.44)) , which results in the symmetry breaking.

We may observe the luminescence quenching in the electric and magnetic field. As was shown in chapter 6, the ground state of the exciton in DQW may become r and k indirect in the presence of both electric and magnetic fields. The probability of recombination is first determined by the overlap integral that describes the probability of finding the electron and hole in the same location. Therefore the probability of recombination substantially decreases for states composed mainly of r-space indirect exciton in comparison with those composed of r-space direct exciton. Second the probability of recombination is governed by the momentum conservation law. Thus the shift of the energy minimum away off the origin in the dispersion relation sharply lowers the probability of recombination of excitons with minimal energy whose consequence is the luminescence quenching, which has already been measured and reported [18]. Due to the discussed sharp drop in recombination probability phonon assisted recombination and transitions between direct and indirect exciton can play a significant role, which may be used for the saser development as is indicated at the end of this chapter and in detail calculated [7].

The evidence of the Bose condensation of diluted exciton gas in AlAs/GaAs DQW was reported by Butov [8] (for higher exciton concentrations Coopers pairs will appear). Such condensation is possible only below the critical temperature T_c. This temperature increases in 2D systems with magnetic field and can reach tens of K for a field of 10 T (shown in Fig. 7.1), which is much better compared to bulk excitons (studied mainly in Cu_2O and Ge). Another important parameter for the condensation is the exciton lifetime. The shift of the minimum of the dispersion relation induces low recombination rates and thus long lifetime. As the calculated results show the maximum depth
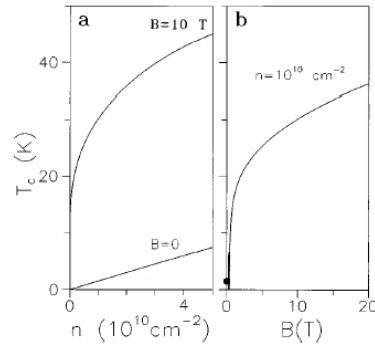
Figure 7.1: Predicted T_c as a function of the exciton density and magnetic field (strong field approximation is considered), taken from [8].

and shift of the energy minimum can be achieved in a sufficiently strong electric field which is however usually stronger than the sample can endure ([2]). Assuming a strong electric field the magnitude of the magnetic field is critical for the achievement of the desired depth of the energy minimum, due to its quadratic dependence on the field. As is discussed in chapter 6, a stronger magnetic field is equivalent to a wider quantum well.

Nevertheless, wider quantum wells have some disadvantages which are not well described by our model. As was estimated before, higher states in z direction should be taken into account for wells wider than 20 nm. Also fluctuation of the potential can play a significant role when more defects appear in the well. Such defects may destroy the coherence of the excitonic liquid and thus instead of a macroscopic state only isolated islands of liquid will appear. Finally excitons in wider DQWs are less bounded which implies a need of very low temperatures.

The last question is the tunnelling. The deepest energy minimum would be achieved with zero tunnelling matrix elements but electrons (holes) could not tunnel to the second well and form the excitonic liquid. The longer the lifetime of the electrons (holes) the smaller the tunnelling elements can be set since the electrons (holes) have enough time to tunnel.

Now we discuss a new type of van Hove logarithmic singularity in the exciton density of states. The density of states of electrons and holes respectively exhibits a singularity in the magnetic field as was for the first time shown by Lyo [1]. This method was then used by Soubusta [2], [19]. The densities of states were calculated for a symmetric DQW in the magnetic field, which is shown in Fig. 7.2b. The critical magnetic field for similar structures as we compute is around 7 T. Orlita [3] calculated the density of states for an asymmetric DQW. The asymmetry was modelled by the DQW structure or by applied electric field. The critical magnetic field for similar structures is in this case slightly stronger (around 9 T), which is depicted in Fig. 7.2a. The photoluminescence spectra were also calculated [20] and showed a reasonable agreement with
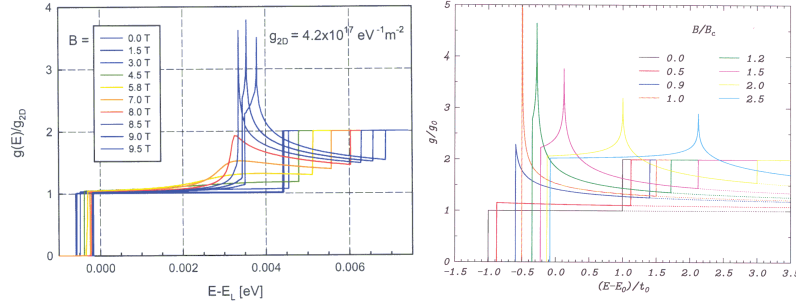
Figure 7.2: Density of states of electrons in asymmetric (a, left) and symmetric (b, right) DQW. Taken from [3] and [2].

measured data. N-type kink is present in the luminescence spectra of symmetric and asymmetric DQW in strong $B_\parallel$ and high electron density. Spectra of the symmetric DQW (a) with a width Γ =0.5 meV and asymmetric DQW (b) with width a Γ =1 meV are shown in Fig. 7.3.

The singularity in the exciton density of states appears only in presence of the resonant electric field and sufficiently strong magnetic field. The value of the resonant field is determined by the condition of the same energies of the direct and indirect exciton, that is to say $F_{res} = (E_d - E_{ind})/de$. A cross section of the parabolas of the direct and indirect exciton is required to observe the singularity. When the singularity coincides with the minimum of the dispersion relation we call such field critical. If the critical magnetic field and resonant electric field are applied, excitons occupy the minimum energy which is now flat (has the second derivative equal to zero). This energy minimum is slightly shifted from the origin (order of 10^{-2} nm^{-1}) and its depth is very small (order of 10^{-2} meV), that's why we would need an extremely low temperature to observe the condensation of excitons. If a magnetic field stronger than the critical one is applied, a region with negative effective mass of the exciton will appear in the dispersion relation as is shown in figures of chapter 6.

The knowledge of the wave functions and dispersion relations enables us to calculate theoretical luminescence spectra for the exciton recombination. Predominantly excitonic luminescence can be seen mainly in undoped samples with low concentration of the electrons and holes. The theoretical spectra calculated in chapter 6 show that the singularity in the density of states manifests significantly. Two peaks composed of the direct and indirect exciton are present for weak magnetic fields (assuming low temperature). As we increase the magnitude of the parallel magnetic field the two energy levels come closer, since the parabola of the indirect exciton is being shifted away off the origin and thus if the critical magnetic field is achieved, only one peak can be observed. If such behaviour of the luminescence spectra was measured our predictions would be verified. The very important question is the width of the Gaussian function
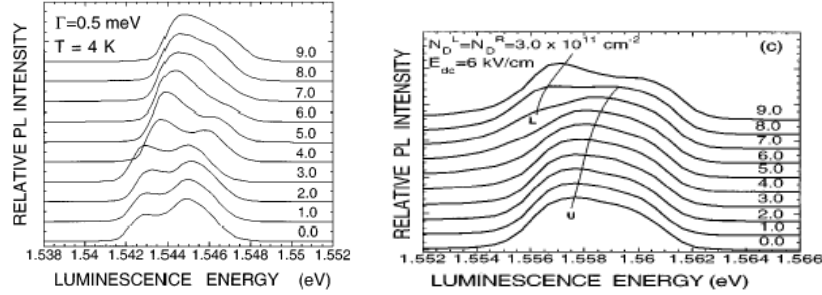
Figure 7.3: Photoluminescence spectra of the free electron-hole recombination for various $B_\parallel$ of the symmetric (a, left) and asymmetric (b, right) DQW, taken from [20].

used in the convolution (4.91). This width is determined by many factors, e.g. by the fluctuation of the gap or by the dynamic disorder. Our choice of the width 0.4 meV lays very strict requirements on the quality of the sample. Luminescence spectra measured on the samples grown at the University of Erlangen and in the Academy of Sciences of the Czech Republic [3] show a Gaussian width of order of meV. Excitonic spectra with such widths would be smeared but some information could be retrieved from the shift of the maxima and from the width of the peaks. It seems that the help of other laboratories could be beneficial to reach a reasonably small width of the Gaussian function to verify our predictions.

The choice of the effective mass of the electron also deserves a discussion. As was shown in Table 2.1 the effective mass of the electron is $0.067m_{e0}$ in bulk GaAs, but since we deal with two-dimensional electron gas we may expect a different effective mass in the xy plane than in the bulk as suggests Ben-Daniel Duke model. Three main influences on the effective mass are discussed in the literature: the nonparabolicity of the conduction band, exchange interaction and correlation effects of electrons, exciton interaction. All of these mechanisms are responsible for the growth of the mass. Nevertheless we use the lower value. The literature for the excitons discusses the value of the parallel effective mass in detail, e.g. various samples were measured [11] and then theoretical calculations were done to interpret the data. The resulting value of the effective mass $0.0421m_{e0}$ was then overtaken by [2]. Calculations done by Soubusta et al. [2] also show reasonable agreement with experiment [19]. Unfortunately the latest measurements done by Orlita [3] indicate that the parallel effective mass can be nearly the same as in the bulk.

The influence of the effective mass on critical magnetic field and resonant electric field is summerized in tables of chapter 6. The heavier particles are, the greater binding energy is. This effect implies a stronger F_{res}. In some cases (e.g. $m_{eff} > 0.1$) F_{res} can be so strong that it may damage the sample, thus increased caution is needed. As the electron becomes heavier in the xy plane, its motion is reduced and the probability of
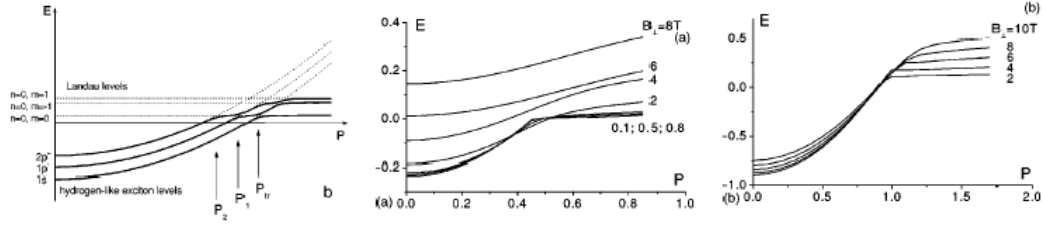
Figure 7.4: Schematic draw of the dispersion relation (a, left) and calculated dispersion relations of indirect (b, middle) and direct (c, right) exciton in various $B_\perp$, taken from [6].

tunnelling into the second well decreases and also the curvature of the dispersion relation decreases resulting in an effectively stronger tunnelling in the resonance. Stronger tunnelling increases the critical magnetic field. In the resonance there is a flat energy level, where a state composed mainly of indirect exciton with momentum $|K_y|_{max}$ continually transforms into a state composed mainly of direct exciton with momentum $|K_y|_{min} \approx 0$. If tunnelling increases, electron alternates the left and right well more frequently. Stronger magnetic field is required to separate such mixed states to get nearly pure indirect exciton state (to localize an electron with a $|K_y|_{max}$ in the well where is not a hole) in the flat energy level, so the plateau is wider with increasing critical magnetic field.

The effect of the perpendicular magnetic field is well-known in the case where the electron-hole interaction is not taken into account. The Landau levels that have the harmonic oscillator structure and are highly degenerate appear. The motion of the electron can be interpreted as a rotation with the cyclotron frequency $\omega_c = \frac{eB_\perp}{m}$ (assuming a symmetric gauge). The mean radius of the rotation in the xy plane is proportional to the momentum and inverse magnitude of the magnetic field, thus a stronger field shrinks the radius. In the exciton case [6] the situation is more complicated. We can distinguish two limiting cases: (i) weak $B_\perp$, where the exciton is hydrogen like and the magnetic field is considered as a perturbation, (ii) magnetic field $B_\perp$ is so strong that the Coulomb interaction is taken as a perturbation to the Landau levels and this kind of behaviour is called magnetoexciton. The average distance of an electron and a hole is $\langle r \rangle \approx K\hbar/eB_\perp$. The situation is schematically shown in Fig. 7.4a. This behaviour can be understood with the help of $\hat{h}(\hat{\mathbf{k}}, \mathbf{K}, \mathbf{r})$ (4.47). This Hamiltonian has two potential like terms with two minima, the first originating from the Coulomb interaction and the second from the parabolic magnetic potential. The energy of the first minimum can be written as $E_{elstat} + E_{kinetic}$ while in the second minimum Landau levels, which are independent of the exciton momentum, hold. Therefore a threshold momentum exists for which the energy of the first minimum is higher than that of the second one and consequently the transition from the hydrogen like exciton to the magnetoexciton occurs. This transition is connected with an increase of the effective mass. A differ-
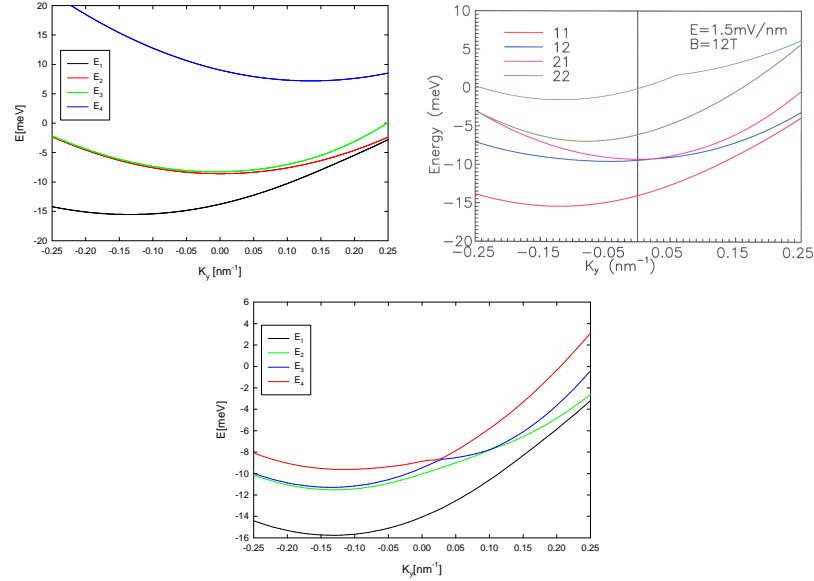
Figure 7.5: Dispersion relation calculated for the same parameters analytically (a, left), using [21] (b, right) and numerically (c, down).

ence between the direct and indirect exciton effective mass will thus exist, since the Coulomb interaction of the indirect exciton is weaker than that of the direct exciton and the Landau levels structure will manifest in a more intensive way. This difference is shown in Fig. 7.4b, c.

As we were not particularly interested in $B_\perp$, our results are not as abundant as we would wish. The results presented in chapter 6 are in a good agreement with those presented in [6]. As is discussed there, the increase of the effective mass of the indirect exciton in the GaAs/AlGaAs DQW is $2.7\times$ experimentally and $2.5\times$ theoretically in $B_\perp = 4$ T. In our case the increase is $2.1\times$ in $B_\perp = 8.9$ T. The deviation is caused mainly by different tunnelling and width of the well (their 11.5 nm and ours 7.5 nm). Nevertheless the qualitative agreement is evident.

We can also discuss a disagreement between models with parabolic and Coulomb potential. Since the parabolic potential increases with the radius more rapidly than the Coulomb one we may expect that the transition between hydrogen like atom and the magnetoexciton will appear in stronger magnetic fields and effective mass of exciton will be lower. This suggestion can be illustrated by figures of chapter 6, where the agreement between analytical and numerical results is good for relatively weak magnetic field $B_\perp < 2$ T and, on the contrary, the agreement is worse for stronger field $B_\perp = 8.9$ T. So if the magnetic field can be treated as a perturbation, the agreement is relatively good since the analytical treatment is adjusted in this way (energy and radius of direct and indirect exciton).
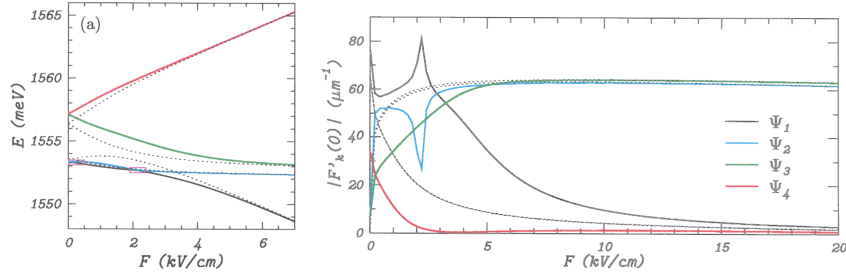
Figure 7.6: Energies of transitions (a, left) and their probabilities (b, right) as a function of electric field in zero electric field, taken from [2].

We will now proceed with a brief discussion of numerical precision and reliability of the results. We have performed many tests to verify if the results are correct and to check that no fatal mistake is present. An older program [21] was used to compare the results and a reasonable agreement was found. The dispersion relations calculated using program [21], and analytical and numerical treatments are plotted in Fig. 7.5. The agreement of the first energy level is excellent. The second level, which corresponds to an excited indirect exciton level for negative momentum, is nearly three times degenerate theoretically. Our analytical calculation does not include any excited levels at all (see Fig. 7.5a). Results of program [21] don't show any degeneracy because of additional demands on the symmetry used there (Fig. 7.5b). Practically twice degenerate level and shifted third level (depicted as the fourth level) are computed numerically (Fig. 7.5c). The energy of this level is higher due to used insufficient range of R, as tests done for the exciton in one well show. The crossovers among excited indirect exciton levels and ground direct exciton level occur for positive momentum and are similar in both numerical calculations. We can conclude that the agreement is very good if we realize that the program [21] is based on a different approach that doesn't work with the expansion of the wave function but the wave function is calculated on a square grid.

We can also look again at figures of section (6.2.4) where the numerically calculated exciton levels and probabilities are discussed. Energy level with zero binding energy without electric field gives us an idea of the indirect exciton spectrum. If we were not limited in the range of R the result could cover in principle the whole spectrum. So we must be cautious in interpreting the results in section (6.2.4) because a more expanded spectrum can be very hardly calculated numerically.

In Fig. 7.6 energies of transitions and their probabilities as a function of electric field in zero magnetic filed are depicted. They are obtained within variation approach [2]. We can qualitatively compare these results with ours in Fig. 6.23 and Fig. 6.24. The energy dependence of the first three levels is similar except from the crossing of levels in Fig. 7.6a, which is caused by used variational method. The excited indirect exciton levels are not considered in [2], which means that the fourth level is composed of the
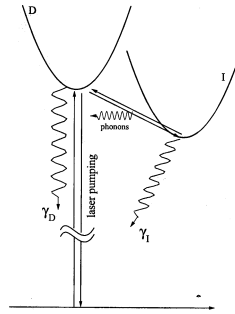
Figure 7.7: Principal scheme of energy levels, D (direct exciton) and I (indirect exciton), taken from [7].

second indirect exciton in contrast with our results. Probabilities are also in good agreement for weak electric field since probabilities of the first and fourth (second and third) level are decreasing (increasing). The differences can be observed for stronger electric field due to missing excited indirect exciton levels. The peak (dip) in the first (second) energy probability is caused by mentioned crossing of levels.

We have found during performed tests that if the lowest energy level is degenerate, the Lanczos method computes very slowly, which is significant in the case of Landau levels and unfortunately also in the case of the singularity where two parabolas, for a certain momentum, are so close that the ground energy is nearly degenerate. The absolute numerical precision is very good since different gauges of the magnetic field give similar results. The difference appears for extreme parameters and also electric field slightly spoils the picture. As expected the stronger magnetic field the more terms of the wave function expansion have to be involved. This expansion enables us to estimate how much the magnetic field rotates the wave functions.

Finally we discuss one of the possible applications of the DQW i.e. the steady stimulated phonon generator (saser or phonon laser). A detailed discussion can be found in [7]. A schematic draw of energy levels is shown in Fig. 7.7. The wave vector of the phonon is determined by the magnitude of the parallel magnetic field and electric field is required to tune the transition direct exciton $\rightarrow$ indirect exciton + phonon into resonance. Thus the magnitude of the electric field is a linear function of the magnitude of the parallel magnetic field. There are several accesible resonances which are connected with different phonon bands. The most suitable are those with a long lifetime. In a typical semiconductor such as GaAs transverse acoustic phonons have the lowest energy and longest lifetime, but their interaction with electronic subsystem is weak and therefore longitudinal acoustic phonons are considered in numerical calculations [7]. The numerical calculation is based on the interaction Hamiltonian in resonant approximation where the laser field is taken into account classically. The master equation for the density operator [22] is taken as a basic equation and is further solved.

Summary

Now we can summarize the results of diploma thesis:

- Hamiltonian for the exciton in the double quantum well in the magnetic and electric field was derived. The tight-binding approximation and the expansion of the wave function into the eigenfunctions of the angular momentum were used. The validity of this approach is discussed.

- A code in C language for the solution of the Hamiltonian was written and the Lanczos method was used to compute eigenvalues and eigenvectors. Various versions of the program were made differing in the treatment of the scalar product and in the gauge of the magnetic field. The deviations between various versions were sufficiently small to confirm a reasonable validity of the obtained results. Additional programs were elaborated to calculate wave function onto square grid, mean values etc.

- The parabolic potential was introduced, which enabled us to pursue further the analytical solution and so to substantially increase the speed of the computations. In the parallel magnetic field, due to the structure of the Hamiltonian matrix, the analytical treatment is sufficient and gives results in a very good agreement with the numerical treatment. The difference can only be seen in strong magnetic fields. Perpendicular magnetic field spoils the agreement but nevertheless analytical treatment gives acceptable qualitative results. The solution of this Hamiltonian was programmed in Fortran with other complementary subroutines for calculations of the density of states and luminescence spectra.

- The calculated dispersion relations and wave functions were used to compute the density of states of the exciton, probability of recombination and even the theoretical luminescence spectra assuming phonon assisted transitions. Two interesting results were discussed in detail: a possible appearance of excitonic liquid and the singularity in the density of states. The calculated theoretical luminescence spectra can be used for verifying the predicted singularity experimentally.

Appendix A

Contents of attached CD-ROM

A CD-ROM with data and programs is attached to the diploma thesis. It has the following structure of directories:

- C files Main program:
  Three C files can be found in this directory. The version with the asymmetric (symmetric) gauge of magnetic field is used in file *NonsymG.c* (*SymG.c*) respectively. The Lanczos method, which can be found in the next directory, is modified in the way the scalar product is computed and extended for the complex matrices. The file Nonscalprod.c is an older version without $B_\perp$ being programmed which uses standard Lanczos method (*lanz2NSP.obj*, *lanz2NSP.for*).

- C project Main program:
  The main program which is a Visual C++ 6.0 project is found here. The files **.lib* are used for the C and Fortran communication. Files *lanz2.f* and *lanz2.obj* contain modified Lanczos method. The modification of the scalar product is done by a new parameter BLOK of the subroutine. This parameter determines the dimension of the subvector for which the the scalar product is calculated. The modification for complex matrices is done by changing the initializing bloc where already computed vectors are not initialized again randomly but are skipped. The dimension of the already computed matrix is also changed. The calling of the Fortran subroutines from C is done according to the Microsoft Power Station manual and thus we write: extern void _stdcall FORTRAN. The present version *2dvodik.c* is for the symmetric gauge. Executable version for symmetric (nonsymmetric) gauge is found in the directory *Symexe* (*Nonsymexe*). The input data of the program are found in the file *vstup.txt* and written in the form shown in Table A.1a. Data should be in one column, but for clarity are divided into three columns. The meanings of quantities are mentioned in text above. *Basis* determines number of basis vectors, 4 for real matrix and 8 for Hermitian.
  There are two kinds of output of the program. The file *energie.txt* contains a table of energies. In the first two lines there are $B_\perp$ and L_z and then for

each $B_\parallel$ there is a table $E(K_x, K_y)$, which is schematically drawn in Table A.1b. Wave functions are stored in output files, whose names consist of parameters of calculation. The structure of the wave function output file is shown in Table A.2. The first two rows should be one column. $IECODE, MMAX, M$ are parameters of the Lanczos method and will be described in Appendix B. E_A^i, E_B^i, E_C^i are energies of ith energy level and E_A is base energy plus diamagnetic shift, E_B is base energy with kinetic term and diamagnetic shift, E_C is base energy of exciton and P^i is probability of recombination. F_{-l}^i is the column of function $f_{-l}(\mathbf{r}, \mathbf{K})$ of ith energy level.

The program computes one set of the wave functions (for the first four levels) about 30-60min on PC with 800MHz processor. If the level crossover occurs computing time can be much longer, in extreme cases it can reach even 24hours. We note that results may be degenerate if $Basis = 8$ and Hamiltonian (4.44) is not complex. If the calculation for various momenta or magnetic fields is done, wave functions are written into files continuously, energies are written in the end.

Table A.1: Structure of the files: *vstup.txt* (a, left) and *energie.txt* (b, right).

$B_\perp$	K_x^{min}	t_e
$B_\parallel^{min}$	K_x^{max}	t_h
$B_\parallel^{max}$	K_x^{step}	E_z
$B_\parallel^{step}$	dr	m_e
K_y^{min}	R	m_h
K_y^{max}	l	L_z
K_y^{step}	$Basis$	ε_r

$B_\perp$			
L_z			
$B_\parallel$			
K_y	K_x	E_i	$\ldots$
$\vdots$	$\ddots$		

Table A.2: Structure of the output wave function file.

$B_\perp$	$B_\parallel$	L_z	E_z	$IECODE$	R	dr	l
$Baze$	$MMAX$	M	T_e	T_h	K_x	K_y	
E_A^i	E_B^i	E_C^i	P^i				
$\vdots$	$\ddots$						
F_{-l}^i	$\ldots$	F_{-l}^i					
$\vdots$	$\ddots$						

- Data:
  This directory has two subdirectories Nonsym and Sym, where calculated data (energies and wave functions) for different gauges are stored.

- Data processed:
  This directory is a storage of processed data: wave functions were recalculated onto the square grid and several mean quantities were figured out. The stored wave functions belong to the ground energy level. The postfix "SS" means that data were calculated by older version of the program and the difference is acceptable.

- Diploma thesis:
  Diploma thesis in TEX and used pictures are stored here. Also pdf file can be found here.

- Fortran Parabola:
  The Program for the analytical solution is stored here. This program lacks any input file since it computes very quickly and direct changes in the code are more comfortable. The marking of the variables is similar to C code.

- Tools for analytical data:
  The two programs can be found in this directory. First one computes the density of states. The dispersion relations are the input data stored in files, which are written in *jmena.txt*. The second one computes the luminescence spectra. The density of states and the probabilities are its input data stored in files written in *jmena.txt* and *jmenaP.txt* respectively. The parameters of the calculation should be adjusted directly in the code of both programs. These programs can also be used for data obtained numerically, but high density of the calculated points is needed for smooth results.

- Tools for numerical data:
  Two important tools for data processing are stored here. The input file of the program *Fcexy* is a wave function computed numerically which is transformed onto the square grid. Input parameters $l, Baze, R, dr$ of the transformation are found in the file *param.txt*. Program *Prumery* computes mean values of Z_e, Z_h, R_{exc} and its input file is a wave function on the square grid. Parameters $Baze, R\sqrt{2}, dr, L_z$, which are needed for the computation, are also stored in *param.txt*. File *jmena.txt* has its traditional meaning (see above).

- Version for unix and linux:
  This directory contains C code files of the main program and subroutines in Fortran (*lanz2.f*, *Sqrt.f*) which should be linked in Unix by C linker using the command:
  gcc SymG.c lanz2.f Sqrt.g -lm
  Executable file *a.out* should be the result.

Appendix B

Lanczos method

The Lanczos method we use was programmed by R.R.Underwood in [23]. The key subroutine called from C code has the following heading.

SUBROUTINE MINVAL(N,Q,PINIT,R,MMAX,EPS,M,D,X,IECODE,N)

Follows the description of parameters for the standard Lanczos method without our modifications:

- N:
  integer variable. The order of the symmetric matrix A whose eigenvalues and eigenvectors are being computed. The value of N should be less than or equal to 1296 and greater than or equal to 2.

- Q:
  integer variable. The number of vectors of length N contained in the array X. The value of Q should be less than or equal to 25, at least one greater than the value of R and less than or equal to N.

- PINIT:
  integer variable. The initial block size to be used in the block lanczos method. If PINIT is negative, then -PINIT is used for the block size and columns M+L,..., M+(-PINIT) of the array X are assumed to be initialized to the initial matrix used to start the block lanczos method. If the subroutine terminates with a value of M less than R, then PINIT is assigned a value -P where P is the final block size chosen. In this circumstance, columns M+1,...M+P will contain the most recent set of eigenvector approximations which can be used to restart the subroutine if desired.

- R:
  integer variable. The number of eigenvalues and eigenvectors being computed. That is, MINVAL attempts to compute accurate approximations to the R least

eigenvalues and eigenvectors of the matrix A. The value of R should be greater than zero and less than Q.

- MMAX:
  integer variable. The maximum number of matrix-vector products A*X (where X is a vector) that are allowed during one call of this subroutine to complete its task of computing R eigenvalues and eigenvectors. Unless the problem indicates otherwise, MMAX should be given a very large value.

- EPS:
  REAL*8 variable. Initially, EPS should contain a value indicating the relative precision to which MINVAL will attempt to compute the eigenvalues and eigenvectors of A. For eigenvalues less in modulus than 1, EPS will be an absolute tolerance. Because of the way this method works, it may happen that the later eigenvalues cannot be computed to the same relative precision as those less in value.

- OP:
  subroutine name. The actual argument corresponding to OP should be the name of a subroutine used to define the matrix A. This subroutine should have three arguments N, U, and V, say, where N is an integer variable giving the order of A, and U and V are two one-dimensional C arrays of length N. If W denotes the vector of order N stored in U, then the statement CALL OP(N,U,V) should result in the vector A*W being computed and stored in V. The contents of U can be modified by this call.

- M:
  integer variable. M gives the number of eigenvalues and eigenvectors already computed. Thus, initially, M should be zero. If M is greater than zero, then columns one through M of the array X are assumed to contain the computed approximations to the M least eigenvalues and eigenvectors of A. On exit, M contains a value equal to the total number of eigenvalues and eigenvectors computed including any already computed when MINVAL was entered. Thus, on exit, the first M elements of D and the first M columns of X will contain approximations to the M least eigenvalues of A.

- D:
  REAL*8 array. D contains the computed eigenvalues. D should be a one-dimensional array with at least Q elements.

- X:
  REAL*8 array. X contains the computed eigenvectors. X should be an array containing at least N*Q elements. X is used not only to store the eigenvectors computed by MINVAL, but also as working storage for the block lanczos method.

On exit, the first N*M elements of X contain the eigenvector approximations - the first vector in the first N elements, the second in the second N elements, etc...

- IECODE:
  integer variable. The value of IECODE indicates whether MINVAL terminated successfully, and if not, the reason why.
  IECODE=0 :successful termination.
  IECODE=1 : the value of N is less than 2.
  IECODE=2 : the value of N exceeds 1296.
  IECODE=3 : the value of R is less than 1.
  IECODE=4 : the value of Q is less than or equal to R.
  IECODE=5 : the value of Q is greater than 25.
  IECODE=6 : the value of Q exceeds N.
  IECODE=7 : the value of MMAX was exceeded before R eigenvalues and eigenvectors were computed.

Bibliography

[1] S. K. Lyo, *Phys. Rev. B* **50** (1994) 4965

[2] J. Soubusta, Thesis, Institute of Physics of Charles University, Prague 1999

[3] M. Orlita, Diploma thesis, Institute of Physics of Charles University, Prague 2002

[4] J. Hu and A. H. MacDonald, *Phys. Rev. B* **46** (1992) 12554

[5] A. A. Gorbatsevich and I. V. Tokatly, *Semicond. Sci. Technol.* **13** (1998) 288

[6] Yu. E. Lozovik, I. V. Ovchinnikov, S. Yu. Volkov, L. V. Butov and D. S. Chemla, *Phys. Rev. B* **65** (2002) 235304

[7] Yu. E. Lozovik, S. P. Merkulova and I. V. Ovchinnikov, *Physics Letters A*, **282** (2001) 407

[8] L. V. Butov and A. I. Filin, *Phys. Rev. B* **58** (1998) 1980

[9] G. Bastard, Wave mechanics applied to semiconductor heterostructures, Paris 1992

[10] J. H. Davies: The physics of low-dimensional semiconductors. Cambridge University Press, Cambridge 1998

[11] T. Westgaard, Q. X. Zhao, B. O. Fimland, K. Johannessen and L. Johnsen, *Phys. Rev. B* **45** (1992) 1784

[12] R. C. Miller, D. A. Kleiman, W. T. Tsang and A. C. Gossard, *Phys. Rev. B*, **24** (1981) 1134

[13] L. P. Gorkov and I. E. Dzyaloshinskii, *Sov. Phys. JEPT* **26** (1968) 449

[14] E. Janke, F. Emde and F. Lösch, Tafeln höherer Funktionen, Stuttgart 1960

[15] A. S. Davydov, Kantová mechanika, Praha 1978

[16] K. Míšek and L. Červinka, Letní škola fysiky pevných látek, Praha 1965

[17] W. H. Press, S. A. Teukolsky, W. T. Vetterling and B. P. Flannery, Numerical recipes in Fortran, Cambridge 1992

[18] A. Parlangeli, P. C. M. Christianen, J. C. Maan, I. V. Tokatly, C. B. Soerensen and P. E. Lindelof, *Phys. Rev. B* **62** (2000) 15323

[19] J. Soubusta, R. Grill, P. Hlídek, M. Zvára, L. Smrčka, S. Malzer, W. Geißelbrecht, and G. H. Döhler, *Phys. Rev. B* **60** (1999) 7740

[20] Danhong Huang and S. K. Lyo, *Phys. Rev. B* **59** (1999) 7600

[21] R. Grill, Program for solving Hamiltonian of exciton in DQW in parallel magnetic field, Nüremberg 1999

[22] V. May and O. Kühn, Charge and energy transfer dynamics in molecular systems: a theoretical introduction, Berlin 2000

[23] R. R. Underwood, Thesis: An Iterative Block Lanczos Method for the C Solution of Large Sparse Symmetric Eigenproblems, 1975